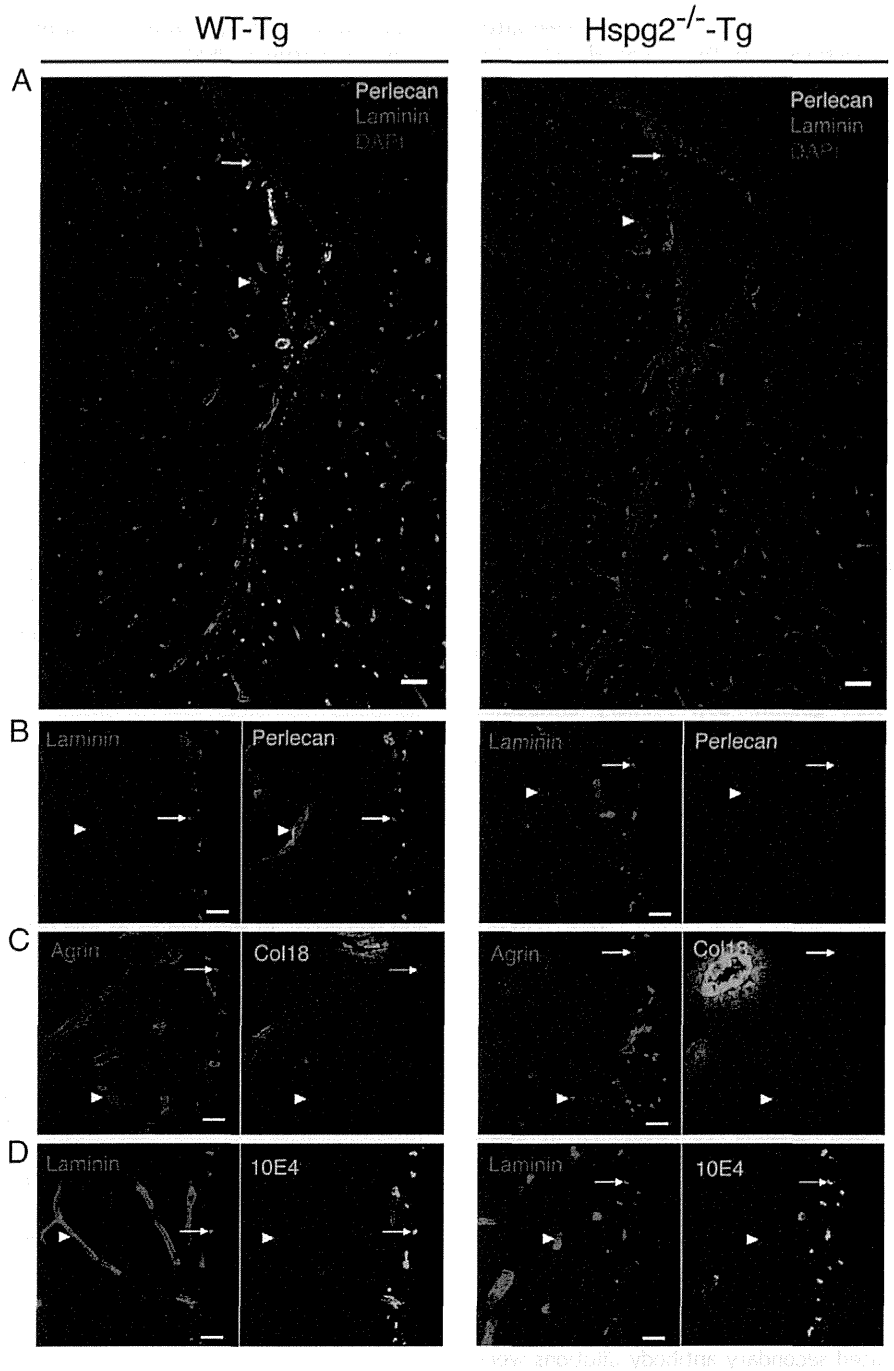

Figure 1 Extracellular matrix content in the SVZ. (A, B) Confocal images of the lateral ventricle of control (WT-Tg) and lethality-rescued perlecan-null mice (Hspg2$^{-/-}$-Tg), showing staining with perlecan (green), laminin-111 (polyclonal, red) and DAPI (blue). Perlecan expression co-localized with laminin on all blood vessels (arrowhead) and fractones (arrow) in the WT-Tg mice, but was absent in the Hspg2$^{-/-}$-Tg. (B, C, D) High magnification of the SVZ. The ependymal wall is on the right of each image and the parenchyma on the left. (C) Agrin (red) display co-localizes with laminin and perlecan while collagen 18 expression (green) is restricted to parenchymal (distance from the ventricle > 50 μm) or large (diameter > 30 μm) blood vessels. Collagen 18 was absent from SVZ capillaries (arrowhead) and from fractones (arrow). (D) The N-sulfated heparan sulfate marker (10E4, green) is strongly present in fractones (arrow) and in SVZ blood vessels (arrowhead), but its expression greatly decreases in the parenchymal blood vessels. Scale bar is 50 mm in A and 20 μm in B, C, and D.

antibodies were rabbit IgG-HRP (Amersham) and mouse IgG-HRP (Amersham). SuperSignal West Dura Chemiluminescent Substrate (Thermo Scientific) was used to detect proteins.

Quantitative real time PCR

RNA from either whole SVZ or neurospheres was extracted using TRIzol reagent (Invitrogen). cDNA was synthetized

using the RT^2 First stand kit from Qiagen. Real time PCR was performed using RT^2 qPCR primer assays and RT^2 SYBR green mastermix from Qiagen on a Fast 7500 Real Time Cycler (Applied Biosystems). Analysis was performed using the web-based application provided by Qiagen.

Quantification and statistical analysis

Analysis was performed using a Leica TCS-SP5 confocal laser scanning microscope. Whole ventricles were reconstructed from pictures taken with 20× plan-apochromat dry objectives (0.7). Serial coronal sections of the SVZ between

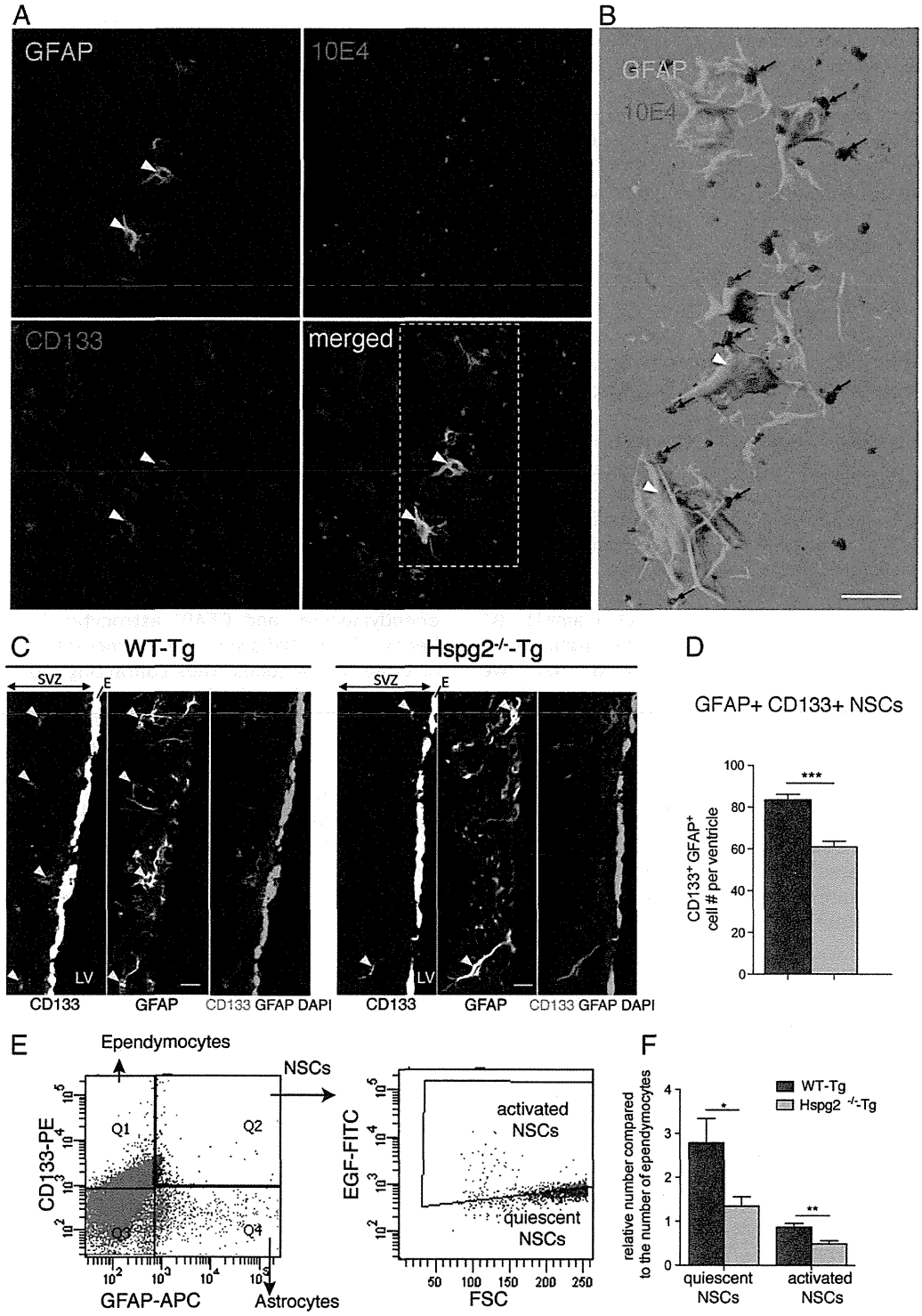

Bregma A 1.1 and Bregma A 0.7 were labeled with either GFAP, CD133, EGF-R, DCX, or BrdU. Cells were counted on images taken from ventricles using ImageJ (ImageJ 1.45 o, Wayne Rasband, NIH, USA). $CD133^+/GFAP^+$ (for type B cells), $EGF\text{-}R^+/GFAP^+$ (for activated type B cells), $EGF\text{-}R^+/GFAP^-$ (for type C cells), and DCX^+ (for type A cells) populations were quantitated by cell type. Serial coronal sections of the RMS between Bregma A 3.2 and Bregma A 3.0 were labeled with DCX, GFAPs, and BrdU. The size of the RMS was assessed by measuring the cluster of DCX^+ cells with ImageJ. Serial coronal sections of the OB between Bregma A 4.3 and Bregma A 4.4 were labeled with NeuN, GFAPs, and BrdU. For neurosphere cultures, statistics were made from 6 wells per condition per animal (from 6 WT-Tg and 4 $Hspg2^{-/-}$-Tg forebrain). Data are presented as the total number of cells per ventricle (mean ± SEM) and analyzed using the Unpaired Student's *t*-test with confidence intervals of 99% or one-way analysis of variance coupled with the Bonferroni post-test (Graph-Pad Prism version 5.0 for Mac OS X, Graph-Pad Software, San Diego, CA).

Results

Perlecan deficiency induces no obvious change in other ECM components in the neurogenic niche

We studied the role of perlecan in NSCs by first comparing the ECM content in the SVZ of $HSPG2^{-/-}$-Tg mice with that of control mice (WT-Tg; Fig. 1). In control mice, perlecan was localized in fractones and all blood vessel basement membranes (SVZ and adjacent neural nuclei). In the $HSPG2^{-/-}$-Tg mice, perlecan was completely absent, but laminin-111 staining, an another basement membrane component which consists of laminin α1 (Lama1), β1 (Lamb1), and γ1 (Lamc1) chains, was still displayed in both fractones and blood vessels (Figs. 1A, B). Next, we investigated other basement membrane heparan sulfate proteoglycans (HSPGs), such as collagen 18 and agrin. While agrin displayed the same patterns as laminin-111 and perlecan, collagen 18 was only expressed in the basement membranes of blood vessels from neural nuclei adjacent to the SVZ and was absent in the fractones and SVZ blood vessel walls of control mice (Fig. 1C).

We also investigated the presence of heparan sulfate (HS) and chondroitin sulfate (CS) chains. Three types of antibodies to heparan sulfate (HS) chains were used: 10E4 (HS epitope including N-sulfated glucosamine) (Fig. 1D), JM403 (HS epitope including N-unsubstituted glucosamine) (Supplemental Fig. 1A), and 3G10 (HS neo-epitope generated by HS chains digestion by heparatinase) (Supplemental Fig. 1B). Immunostaining with these antibodies showed similar localizations of HSs. They were all strongly expressed in fractones and in SVZ blood vessels, but their expression was substantially weaker in blood vessels outside the SVZ of both WT-Tg and $Hspg2^{-/-}$-Tg mice. Antibody CS-56 to CS types A and C did not stain either fractones or most of the SVZ blood vessels, but did stain blood vessels of the neural nuclei adjacent to the SVZ and the pericellular matrix of SVZ cells (Supplemental Fig. 1C). The absence of perlecan did not cause any obvious visible change in the expression of these HS and CS chains in the SVZ. These results suggest that, in the absence of perlecan, basement membranes exist and other HS chain-containing basement membrane components, such as agrin, are present in fractones and in most SVZ blood vessels.

Perlecan presence is critical for neural stem cell maintenance and for neurogenesis in the SVZ

We next investigated the maintenance of NSCs and neurogenesis in the SVZ of $Hspg2^{-/-}$-Tg mice. We characterized the cell identity with several cell type markers, such as GFAP, CD133, EGF-R, and DCX. CD133, also known as Prominin 1 (PROM1), is a marker of cancer stem cells and has been used to identify NSCs in both humans and rodents (Uchida et al., 2000; Corti et al., 2007; Mirzadeh et al., 2008). We used CD133 as a marker for NSCs, in addition to another NSC marker, GFAP. This combination allowed us to distinguish NSCs from $CD133^+$ ependymocytes and $GFAP^+$ astrocytes (Fig. 2A, arrowheads). These NSCs sent many processes in the direction of close-by fractones, thus contacting most fractones in their vicinity (Fig. 2B).

We found a 27% decrease in the number of $CD133^+$ NSCs in $Hspg2^{-/-}$-Tg mice (WT-Tg: 83.55 ± 2.60 $CD133^+/GFAP^+$ cells per ventricle, $Hspg2^{-/-}$-Tg: 61.06 ± 2.60; Figs. 2C,D). This result was confirmed by flow cytometry analysis of the SVZ. Both quiescent ($CD133^+$ $GFAP^+$ $EGF\text{-}R^-$) and activated ($CD133^+$ $GFAP^+$ $EGF\text{-}R^+$) NSCs were significantly reduced in the $Hspg2^{-/-}$-Tg (Figs. 2E,F). The number of activated type B cells was reduced by 53% in the absence of perlecan (WT-Tg: 5.06 ± 0.22 $EGF\text{-}R^+/GFAP^+$ cells per ventricle; $Hspg2^{-/-}$-Tg:

Figure 2 Neural stem cell maintenance in perlecan null mice. (A) Confocal image of the surface of the ependymal wall of the lateral ventricle stained with CD133, GFAP and heparan sulfate chains (10E4) reveals fractones (10E4 staining) in the vicinity of $CD133^+GFAP^+$ NSCs (arrowheads). (B) Shadow projection of a Z-stack of the insert in A (realized with Imaris software) shows NSCs contacting numerous fractones (arrows). (C) Confocal image of the SVZ (striatum side) displaying CD133 and GFAP staining in WT-Tg and $Hspg2^{-/-}$-Tg. CD133 is expressed strongly by ependymocytes and is also present in SVZ NSCs. GFAP is expressed by SVZ astrocytes and NSCs. We discriminated SVZ NSCs by counting positive cells for both CD133 and GFAP in the subependymal layer (arrows show four double positive cells in the image for WT-Tg SVZ and two in the image for $Hspg2^{-/-}$-Tg SVZ. (D) Bar chart displaying the total number $CD133^+GFAP^+$ NSCs per ventricles in WT-Tg and $Hspg2^{-/-}$-Tg. In the $Hspg2^{-/-}$-Tg mice $CD133^+GFAP^+$ NSC number was decreased by 27%. The data are expressed as mean ± SEM (n = 5, *** indicates P-value of $P < 0.0001$; Student's *t*-test). (E) Dot plot depicting the characterization of NSCs by flow cytometry analysis and the separation of activated NSCs (EGF + fraction) and quiescent NSCs (EGF-fraction). (F) Bar chart displaying the number of quiescent NSCs and activated NSCs (for one hundred ependymocytes CD133+ GFAP-) in WT-Tg and $Hspg2^{-/-}$-Tg SVZ assessed by flow cytometry analysis. Both quiescent and activated NSCs are reduced in the $Hspg2^{-/-}$-Tg brain. The data are expressed as mean ± SEM (n = 3, * indicates P-value of $P = 0.0159$, ** indicates P-value of $P = 0.0069$; Student's *t*-test). Scale bar: 10 μm. SVZ: subventricular zone; E: ependyma; LV: lateral ventricle.

2.35 ± 0.17; Fig. 3B). The number of type C cells was decreased by 20% (WT-Tg: 37.53 ± 2.01 EGF-R$^+$/GFAP$^-$ cells per ventricle; Hspg2$^{-/-}$-Tg: 29.94 ± 1.14; Fig. 3C).

We also analyzed the neuroblast population (DCX$^+$ cells) and proliferating cells in the SVZ. The number of neuroblasts decreased by 18% in the absence of

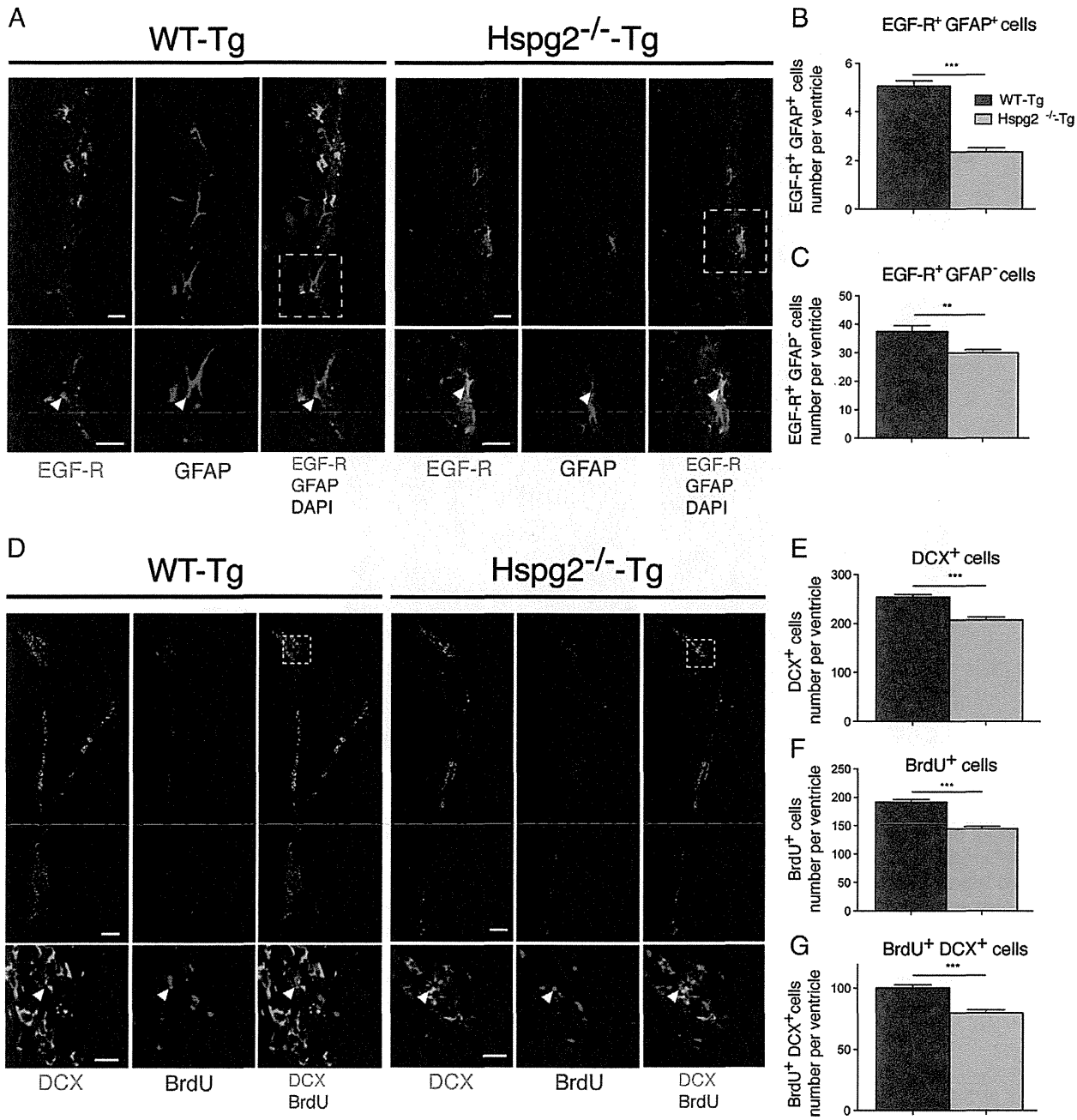

Figure 3 Neurogenesis in the SVZ of perlecan null mice. (A) Confocal image of the SVZ (striatum side) showing EGF-R, GFAP, and DAPI staining in WT-Tg and Hspg2$^{-/-}$-Tg mice. The insert shows examples of double positive EGF-R$^+$GFAP$^+$ (activated type B cells) at a higher magnification (arrowhead). (B) Bar chart indicates the total number of EGF-R$^+$GFAP$^+$ cells (activated type B cells) per ventricle in WT-Tg and Hspg2$^{-/-}$-Tg mice. In the Hspg2$^{-/-}$-Tg mice, EGF-R$^+$GFAP$^+$ cell numbers were decreased by 53%. (C) Bar chart displaying total number EGF-R-GFAP$^+$ cells (type C cells) per ventricle in WT-Tg and Hspg2$^{-/-}$-Tg mice. In the Hspg2$^{-/-}$-Tg mice, EGF-R$^+$GFAP$^+$ cell numbers were decreased by 20%. (D) Reconstructed lateral ventricle from a confocal image displaying DCX and BrdU staining. Insert shows the horn of the lateral ventricle at a higher magnification. Arrowhead shows a double-positive DCX$^+$BrdU$^+$ cell. (E, F, G) Bar chart indicates the total number of DCX$^+$ cells (type A cells, E), BrdU$^+$ cells (proliferating cells), and DCX$^+$BrdU$^+$ cells (newly born type A cells) per ventricle in WT-Tg and Hspg2$^{-/-}$-Tg mice. In the Hspg2$^{-/-}$-Tg mice, DCX$^+$ cell numbers decreased by 18%, proliferating cell numbers decreased by 25%, and newly formed type A cell numbers decreased by 20%. The data are expressed as mean ± SEM (n = 5, *** indicates P-value of $P < 0.0001$; ** indicates P-value of $P < 0.01$; Student's t-test). Scale bar: 10 μm in A, 100 μm in D and 30 μm in insert in D.

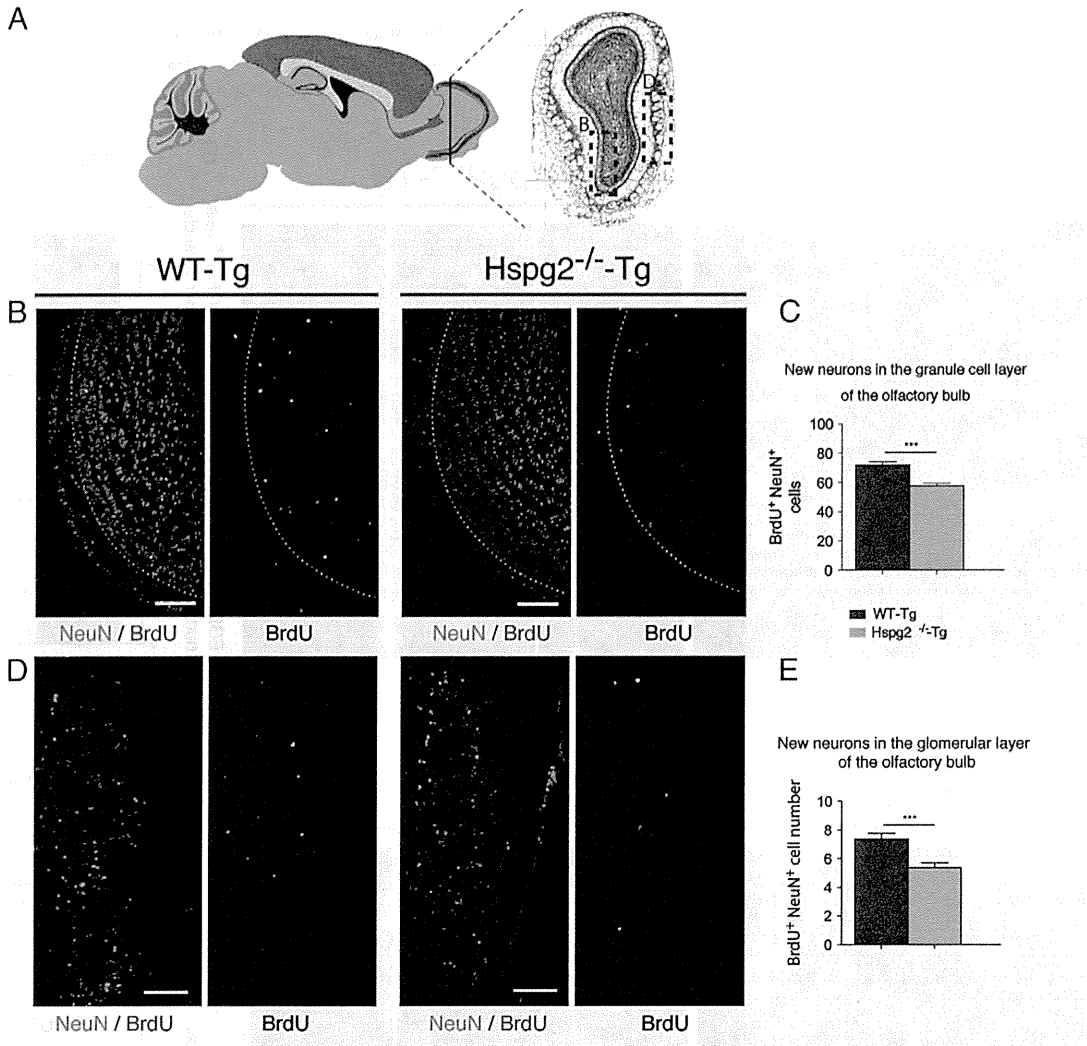

Figure 4 New neurons in the olfactory bulb in perlecan null mice. (A) Drawing of a sagittal section of a mouse brain showing the localization of the coronal section (Nissl staining showing the lateral ventricle at bregma A +4). Insert depicts the area where confocal images in Fig. 5B and D were taken. (B) Confocal image of the granule cell layer (GCL) of the OB displaying NeuN and BrdU staining in WT-Tg and Hspg2$^{-/-}$-Tg mice. Dotted lines show the boundary of the GCL. Overall, 95% of BrdU$^+$ cells co-localized with the mature neuronal marker NeuN. (C) Bar chart indicates the total number of BrdU$^+$NeuN$^+$ cells (new neurons) in one field (0.624 μm^2) of the GCL (5B represent half of a field). The number of proliferating cells in the GCL decreased by 20% in Hspg2$^{-/-}$-Tg mice. (D) Confocal image of the glomerular layer (GL) of the OB indicates NeuN and BrdU staining in WT-Tg and Hspg2$^{-/-}$-Tg mice. (E) Bar chart indicates the total number of BrdU$^+$NeuN$^+$ cells (new neurons) in one field (0.312 μm^2 as shown in 5D) of the GL. The number of proliferating cells in the GL decreased by 27% in Hspg2$^{-/-}$-Tg mice. The data are expressed as means ± SEM (n = 5, *** indicates P-value of $P < 0.0001$; Student's t-test).

perlecan (WT-Tg: 253.80 ± 5.52 DCX$^+$ cells per ventricle; Hspg2$^{-/-}$-Tg: 207.3 ± 6.04; Fig. 3E). To detect newly formed neuroblasts, we analyzed BrdU-positive cells in the SVZ 48 h after a single BrdU injection into the animals. We found that the number of proliferating BrdU$^+$ cells decreased by 25% (WT-Tg: 191.8 ± 4.09 BrdU$^+$ cells per ventricle; Hspg2$^{-/-}$-Tg: 144.6 ± 3.92; Fig. 3F). The number of newly formed neuroblasts (DCX$^+$/BrdU$^+$) also decreased by 20% in the absence of perlecan (WT-Tg: 100.30 ± 2.54 DCX$^+$ cells per ventricle; Hspg2$^{-/-}$-Tg: 79.79 ± 2.45; Fig. 3G). These results indicate that the NSC population was reduced in the perlecan-deficient SVZ, which ultimately resulted in a decrease in neurogenesis.

Fewer new neurons integrate into the olfactory bulb in the Hspg2$^{-/-}$-Tg mice

After exiting the SVZ, neuroblasts migrate toward the olfactory bulb in the rostral migratory stream (RMS). Thus, we followed the fate of the generated neuroblasts 4 weeks after BrdU injection. We found that the RMS size was reduced by 25% in the absence of perlecan (Supplemental Fig. 2 B, C), in accordance with the lower number of neuroblasts generated in the SVZ. Moreover, the majority of BrdU$^+$ cells already exited the RMS and stopped expressing DCX. These cells were detected in the granule cell layer (GCL) adjacent to the RMS (Supplemental Fig. 2D). The numbers of BrdU + cells

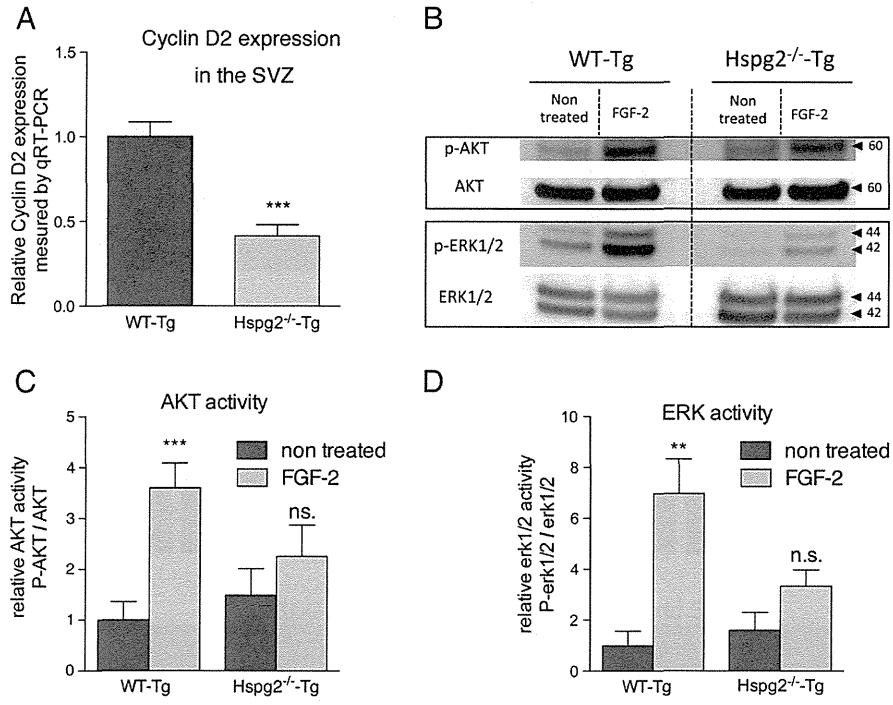

Figure 5 Cyclin D2 expression and FGF-2-induced activation of Akt and Erk1/2 pathways *in vivo*. (A) Bar chart indicates lower cyclin D2 expression in the SVZ of Hspg2$^{-/-}$-Tg compared to WT-Tg mice (n = 4, *** indicates P-value of $P < 0.0001$). (B) Whole SVZ lysates were immunobloted with the indicated antibodies. WT-Tg and Hspg2$^{-/-}$-Tg mice were either not treated or ICV-injected with 0.5 μg of FGF-2 for 30 min prior to sacrifice. (C, D) Bar charts indicate that FGF-2 induced a significant increase of the activation of Akt and Erk1/2 pathways in the WT-tg but not in the Hspg2$^{-/-}$-Tg mice. The data are expressed as means ± SEM (n = 3, *** indicates P-value of P = 0.0007, ** indicates P-value of P = 0.0038; Student's t-test).

in the GCL adjacent to the RMS were reduced by 18% in the absence of perlecan (WT-Tg: 56.12 ± 1.39 BrdU$^+$/NeuN$^+$ cells; Hspg2$^{-/-}$-Tg: 45.76 ± 2.46; Fig. 4E).

We then investigated the nature of the BrdU$^+$ cell population in the olfactory bulb. We found that most BrdU$^+$ cells had begun to express the neuronal marker NeuN (95% of BrdU$^+$ cell co-expressed NeuN). These new neurons (BrdU$^+$/NeuN$^+$) were detected in the GCL (Fig. 4B) and the GL (Fig. 4D). We observed a reduction in the integration of new neurons in the GCL (WT-Tg: 72.15 ± 1.96 BrdU$^+$/NeuN$^+$ cells; Hspg2$^{-/-}$-Tg: 57.73 ± 1.79; Fig. 4C) and the GL (WT-Tg: 7.37 ± 0.40 BrdU$^+$/NeuN$^+$ cells; Hspg2$^{-/-}$-Tg: 5.36 ± 0.34; Fig. 4E) in the perlecan-deficient brain. These data confirmed that the decrease of CD133$^+$ NSCs observed in the perlecan-deficient brain leads to fewer new neurons in the olfactory bulb. Our results show that perlecan is necessary for the maintenance of the CD133$^+$ NSC population, and for neurogenesis.

Perlecan is necessary for FGF-2-induced activation of Akt and Erk1/2 pathways in the subventricular zone

To understand the reason why early events of neurogenesis were impaired in the absence of perlecan, we investigated the expression level of cyclin D2. Cyclin D2 is a protein regulating cell cycle progression in NSPCs. Its expression is necessary for entry into the G_1/S phase of the cell cycle. We found that cyclin D2 expression was significantly reduced in the Hspg2$^{-/-}$-Tg mice (Fig. 5 A). Perlecan is widely recognized as an HSPG modulator of FGF-2 signaling (Aviezer et al., 1994; Rapraeger, 1995). To understand how perlecan regulates FGF-2 activity in the neural stem cell niche, we investigated the activation of the Akt and Erk1/2 pathways in the SVZ after FGF-2 ICV injection. We found that FGF-2 stimulation induced increased phosphorylation of both Akt and Erk1/2 proteins in the WT-Tg mice. However, FGF-2 stimulation failed to activate these two pathways in the absence of perlecan (Fig. 5 B–D). These results indicate that perlecan is necessary for the FGF-2-induced activation of Akt and Erk1/2 pathways *in vivo*.

Neural stem cells express perlecan and can bind FGF-2 *in vitro*

To further investigate the role of FGF-2 on NSCs, we cultivated neurospheres from the cortex of both E16.5 WT-Tg and Hspg2$^{-/-}$-Tg mice. Perlecan was detected in the neurospheres, where its localization was found on the surface of cells that also expressed N-sulfated HS chains (10E4 epitope, Fig. 6A). These cells often coexpressed the stem cell marker CD133 (Fig. 6B). Furthermore, biotinylated FGF-2 was mainly captured by those cells expressing perlecan, 10E4, and CD133. Over 80% of cells that captured FGF-2 also expressed perlecan. However, FGF-2 was not found on the surface of cells expressing chondroitin sulfate chains (Fig. 6C, arrows). This indicates that within the neurosphere CD133$^+$ putative NSCs are surrounded by ECM molecules, such as perlecan and HS chains, and are able to capture FGF-2. To confirm the differentiation potentials of neurospheres, we cultured the primary neurospheres for an additional seven days in the absence of a growth factor.

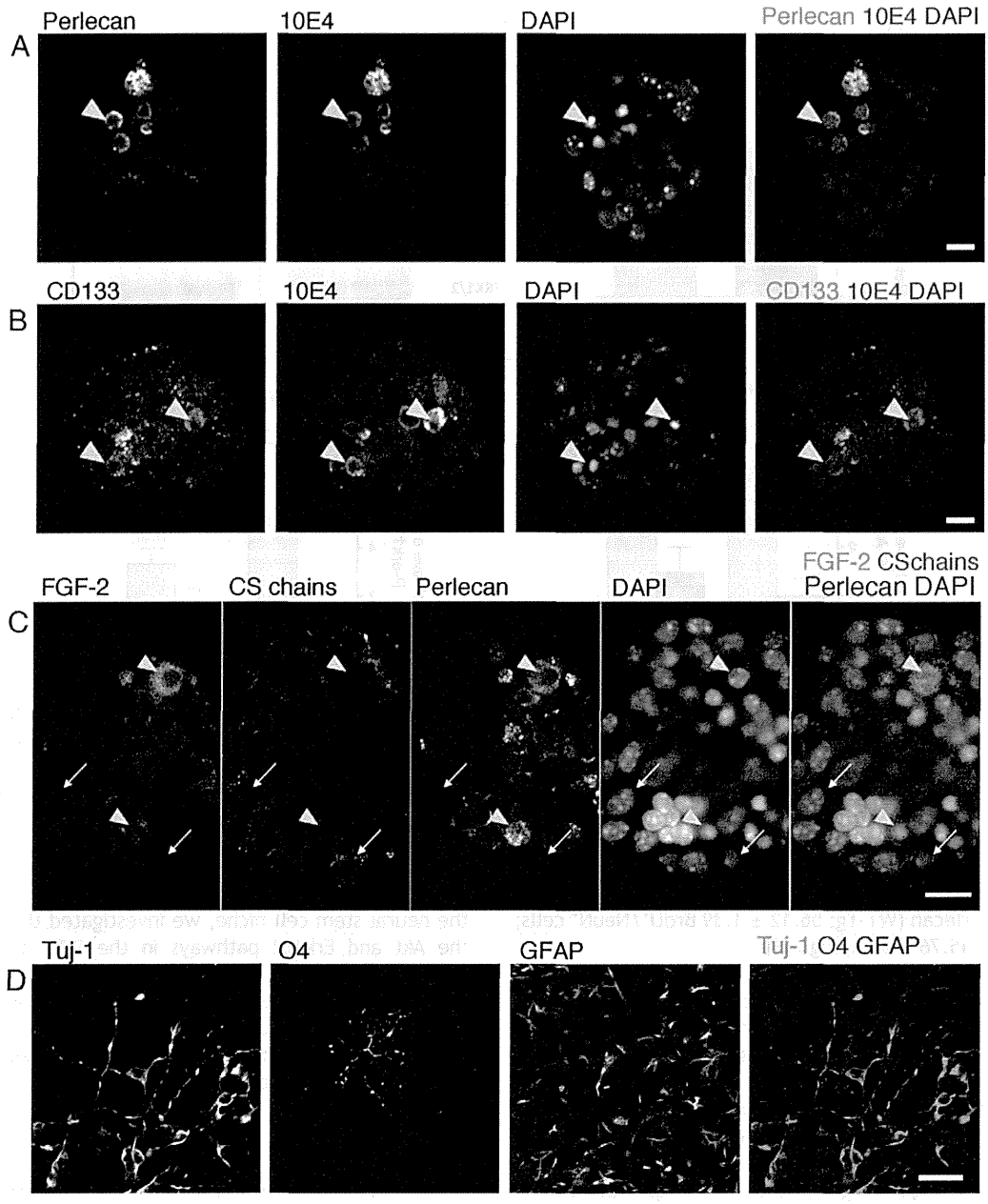

Figure 6 $CD133^+$ NSCs in neurospheres express perlecan and heparan sulfate chains and can capture FGF-2. (A–C) Confocal images of E16.5 WT-Tg neurosphere stained for perlecan, heparan sulfate chains (10E4), CD133, FGF-2, and chondroitin sulfate chains (CS56). Arrowheads point out cells within the neurosphere that co-express perlecan and 10E4 in A, CD133 and 10E4 in B. In C, arrowhead shows that FGF-2 localizes to the surface of cells expressing perlecan but not on the surface of cells that only express chondroitin sulfate chains (arrows). (D) Confocal image of a differentiated neurosphere displaying neurons (stained with Tuj-1), an oligodendrocyte (stained with O4), and astrocytes (stained with GFAP). Scale bar: 10 μm.

We were able to detect oligodendrocytes, neurons, and astrocytes (Fig. 6D).

Perlecan regulates FGF-2 promotion of neurosphere formation

Since FGF-2 activated Akt and Erk1/2 pathways in the SZV of WT-Tg mice but not $Hspg2^{-/-}$-Tg mice, we investigated the effect of FGF-2 on the formation of neurospheres derived from the cortex of both E16.5 WT-Tg and $Hspg2^{-/-}$-Tg mice at different concentrations of FGF-2 (0, 20 and 200 ng/ml). The number of neurospheres from WT-Tg mice increased accordingly due to increases in the FGF-2 concentrations. However, FGF-2 concentrations had no effect on the number of neurospheres from $Hspg2^{-/-}$-Tg (Fig. 7A). We also found that $Hspg2^{-/-}$-Tg neurospheres were significantly smaller (WT-Tg: 83.3 ± 1.58 μm; $Hspg2^{-/-}$-Tg: 52 ± 0.86 μm, Fig. 7B). The basal phosphorylation level of Akt in $Hspg2^{-/-}$-Tg neurospheres was slightly less than that in WT-Tg neurospheres,

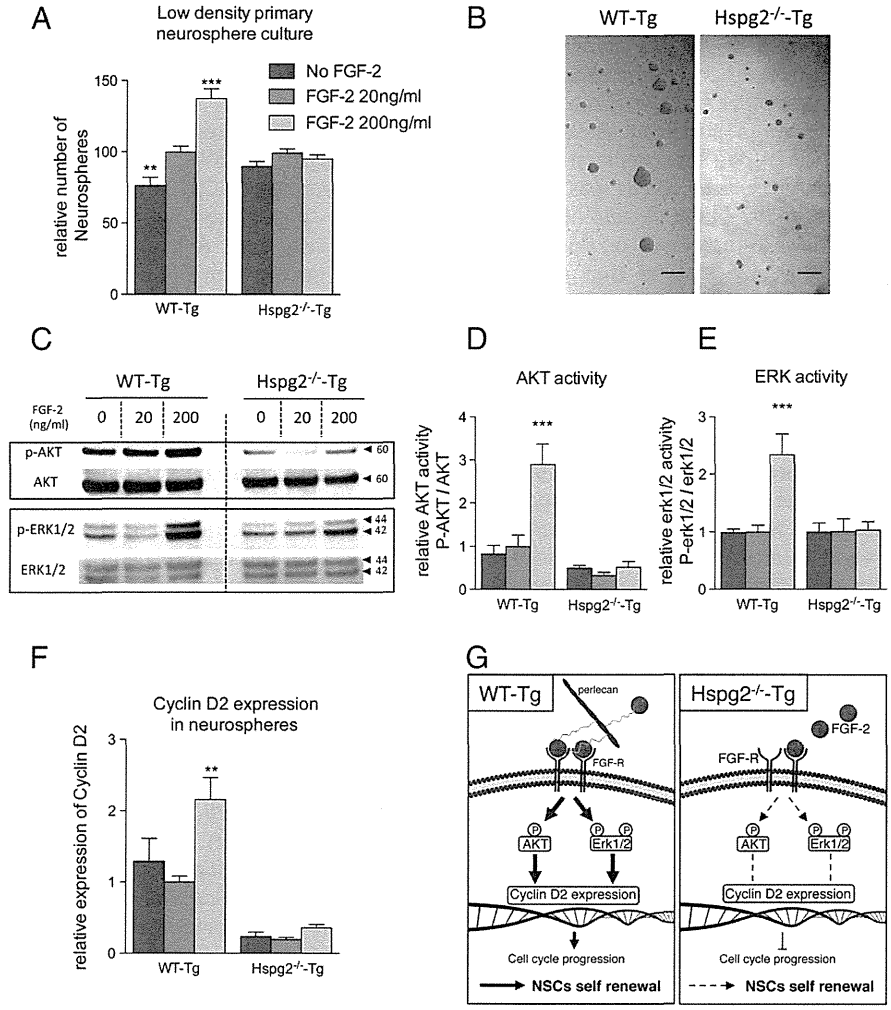

Figure 7 Perlecan is necessary for FGF-2 promotion of neurosphere formation. (A) Low density primary neurosphere culture in the presence of EGF (20 ng/ml) and different concentrations of FGF-2 (0, 20, 200 ng/ml). In the absence of perlecan, FGF-2 fails to promote neurosphere formation. The data are expressed as means ± SEM (n = 6, *** indicates P-value of $P < 0.0001$; ** indicates P-value of $P < 0.001$; one way analysis of variance followed by Bonferroni's multiple comparison test). (B) Bright field images of the primary neurosphere culture after 1 week *in vitro*. The average size of neurospheres from perlecan-deficient brain is significantly smaller (WT-Tg: 83.3 ± 1.58 μm; Hspg2$^{-/-}$-Tg: 52 ± 0.86 μm; $p < 0.0001$). Scale bar: 150 μm. (C) Neurospheres were immunoblotted with indicated antibodies. (D, E) FGF-2 stimulation of Akt and Erk1/2 pathways is impaired in the absence of perlecan. (F) In the absence of perlecan, cyclin D2 expression is significantly reduced and is not responsive to FGF-2 stimulation. (D–F) The data are expressed as means ± SEM (n = 3, *** indicates P-value of $P < 0.001$, ** indicates P-value of $P = 0.0019$. (G) Proposed mechanism of the perlecan function in FGF-2-dependent neurogenesis. In the presence of perlecan, FGF-2 activates Akt and Erk1/2 pathways and increases cyclin D2 expression leading to the progression of the cell cycle thus allowing NSCs self renewal and neurogenesis. In absence of perlecan, this series of event is greatly impaired.

whereas the basal phosphorylation level of Erk1/2 was similar between Hspg2$^{-/-}$-Tg and WT-Tg neurospheres (Fig. 7C–E). The addition of FGF-2 at a high concentration (200 ng/ml) to the culture induced a significant increase in the phosphorylation levels of both Akt and Erk1/2 in the WT-Tg mice, whereas this FGF effect was much less in Hspg2$^{-/-}$-Tg mice (Fig. 7C–E). Furthermore, the expression of cyclin D2 was less in Hspg2$^{-/-}$-Tg neurospheres than the level in WT-Tg neurospheres (Fig. 7F). The high concentration of FGF-2 also significantly increased cyclin D2 expression in WT-Tg neurospheres. In Hspg2$^{-/-}$-Tg neurospheres, the level of induction of the cyclin D2 expression by FGF was less than that in WT-Tg neurospheres (Fig. 7 F). Hence, we propose in Fig. 7 G that perlecan is necessary for FGF-2 to activate the Akt and Erk1/2 pathways, thus leading to cyclin D2 expression, cell cycle progression, and ultimately NSCs self-renewal and proliferation. Taken together, our results strongly suggest that perlecan affects FGF-2 dependent maintenance of NSCs.

Discussion

Extracellular matrix in the neurogenic niche of Hspg2$^{-/-}$-Tg mice

We previously reported some disparities in the composition of ECM components in fractones and nearby capillaries when

these were compared with blood vessels outside the SVZ. Laminin α1 (Lama1) is present in large (>25 μm of diameter) arteries and arterioles, while other basement membrane molecules, such as laminin β1 (Lamb1), perlecan, collagen IV, and nidogen, are present in all blood vessels and in fractones (Mercier et al., 2002). We also reported that 10E4 antibody staining for heparan sulfate chains was primarily observed in fractones and in SVZ blood vessels (Kerever et al., 2007; Mercier and Arikawa-Hirasawa, 2012; Douet et al., 2013). In the present study, we showed that agrin was expressed in fractones and in blood vessel basement membranes (as we previously reported for perlecan), but that collagen 18 was only expressed in blood vessels from adjacent neural nuclei. We found that all three different antibodies to HS chains stained fractones and SVZ blood vessels, and these showed no obvious changes in their expression patterns in the absence of perlecan. It is unlikely that collagen 18 compensates for perlecan loss to maintain those HS chains because it was absent in the neurogenic niche. Agrin most likely accounts for this staining, since it is a proteoglycan that bears heparan sulfate chains. Therefore, our data suggest that HS chains and/or the protein core of perlecan are involved in neurogenesis because the absence of perlecan greatly impaired neurogenesis.

Neural stem cell maintenance

A specific marker for the identification of NSCs is still lacking because most recognized markers are also expressed by other cell types. Therefore, we used a combination of CD133 and GFAP, two markers present in NSCs. GFAP and CD133 can be found in SVZ astrocytes and in ependymocytes, respectively. The use of both markers allowed us to characterize a specific cell population. Type B cells frequently penetrate the ependymal layer to contact the ventricle (Mirzadeh et al., 2008; Shen et al., 2008). Indeed, we observed that $CD133^+GFAP^+$ cells often extended processes contacting the ventricle where CD133 was absent in ependymal cells (Fig. 2B). One possible explanation for the decrease in $CD133^+$ NSCs in the perlecan-deficient brain may be that perlecan serves as a survival factor. Staining for an apoptosis marker, single-stranded DNA (SSDNA), showed negligible cell death in the SVZ of WT-Tg and $Hspg2^{-/-}$-Tg mice (Supplemental Fig. 4), similar to that in the SVZ of wild type mice as reported (Shen et al., 2008). Notably, some $CD133^-$ cells also share NSC properties (Sun et al., 2009), and CD133 is expressed in type B1 cells, a subpopulation of type B cells that function as NSCs (Mirzadeh et al., 2008). Both NSC populations ($CD133^+GFAP^+$ and $CD133^-GFAP^+$) may therefore coexist in the adult SVZ. However, the necessity of CD133 expression for differentiation is unknown. Sun et al. reported that the $CD133^-$ NSC population is mainly in the G_0/G_1 phase, while the $CD133^+$ NSC population is evenly split between G_0/G_1 and G_2/M. Moreover, when cultured, the progeny of this $CD133^-$ NSC population reacquired CD133. This suggests that a transition from a quiescent $CD133^-$ NSC into a $CD133^+$ NSC is possible in vitro.

Cyclin D2 is a G_1 active cyclin that is necessary for the progression of the cell cycle. The lack of functional cyclin D2 leads to a critically impaired adult neurogenesis (Kowalczyk, 2004). Here we observed that in the absence of perlecan, cyclin D2 expression was significantly reduced both *in vivo* and *in vitro*. These results further suggest that perlecan is necessary for the cyclin D2-mediated progression of the NSC cell cycle.

We observed a reduction in the numbers of type C and type A cells in the SVZ, but this reduction was proportional to the decrease in CD133 + GFAP + NSCs in the absence of perlecan. If perlecan was involved in the differentiation process into type A cells, we would have expected a stronger decrease in the population of new neuroblasts in the SVZ. Our results suggest that perlecan was not necessary to amplify type C cells or to differentiate into type A cells, but that it was necessary to maintain the population of NSCs.

We found that the decrease in the size of the RMS in $Hspg2^{-/-}$-Tg mice was equivalent to the decreased number of type A cells exiting the SVZ. Therefore, perlecan may not be necessary for the migration of neuroblasts. Once neuroblasts arrive in the olfactory bulb, the majority of them start to differentiate into mature neurons in the granule cell layer. Others migrate further to the glomerular layer, where they differentiate into periglomerular neurons. We observed a decrease in the integration of new neurons into the olfactory bulb in both the granule cell layer and the glomerular layer in $Hspg2^{-/-}$-Tg mice. These results are consistent with the decrease in numbers of $CD133^+GFAP^+$ NSCs, which resulted in a decrease in new neurons integrating into the olfactory bulb.

Perlecan is involved in angiogenesis through the binding and modulation of growth factor activity (Aviezer et al., 1994; Ishijima et al., 2012). Removal of perlecan HS chains causes impaired tumor angiogenesis and tumor growth (Zhou, 2004). $CD133^+$ cancer stem cells have been identified as a critical cell population for resistance to chemotherapy (Liu et al., 2006). Our findings in the present study that perlecan is critical for $CD133^+$ NSCs, open the question of whether perlecan plays a role in the maintenance of $CD133^+$ cancer stem cells.

FGF-2 stimulation of neurogenesis is impaired in the absence of perlecan

In this study, we showed that the ability to form neurospheres in response to FGF-2 stimulation was less effective in the absence of perlecan. Furthermore, the activation of Akt and Erk1/2, two major downstream signaling pathway of FGF-2, was critically impaired both *in vivo* and *in vitro* in the absence of perlecan. Furthermore, cyclin D2 expression which has been shown to be positively regulated by the activation of the Akt and Erk pathways (Dey et al., 2000; Fatrai et al., 2006), also failed to increase following FGF-2 stimulation in neurospheres derived from perlecan-deficient mice. Hence, we proposed that the absence of perlecan critically affects FGF-2 signaling, which results in reduced cyclin D2 expression and eventually a significant decrease in the NSC self-renewal and neurogenesis.

Chondroitin sulfate (CS) glycosaminoglycans have also been suggested to play a role in FGF-2 signaling (Filla et al., 1998; Hagihara et al., 2000; Sirko et al., 2010). We previously reported that fractones and SVZ blood vessels specifically capture FGF-2 from the extracellular milieu (Kerever et al., 2007). However, we did not detect CS chains in the fractones and in the SVZ blood vessels of either the WT-Tg or the $Hspg2^{-/-}$-Tg mice. Furthermore, FGF-2 localization was

correlated with cells expressing perlecan but not with cells expressing CS chains in neurospheres. These results suggest that perlecan is the major proteoglycans responsible for the management of heparin-binding growth factors, such as FGF-2, in the neurogenic niche.

An extracellular matrix niche for neurogenesis

Previous studies have introduced the concept of the vascular niche for neurogenesis in the SVZ (Shen et al., 2008; Tavazoie et al., 2008; Kojima et al., 2010). At the vascular basement membrane interface, the fate of NSCs is influenced by signals diffusing from endothelial cells (Shen et al., 2008), and also by signals traveling through the blood–brain barrier (Tavazoie et al., 2008). The contact between $\alpha 6\beta 1$ integrins of NSCs and laminin in the blood vessel basement membrane is crucial for the positioning and proliferation of NSCs (Shen et al., 2008; Tavazoie et al., 2008). In addition, fractones have been implicated as crucial niche components that are tightly associated with NSCs (Mercier et al., 2002, 2003; Kerever et al., 2007; Mercier and Arikawa-Hirasawa, 2012; Douet et al., 2013). Growth factors, such as FGF-2 and BMP-7, in the cerebrospinal fluid may penetrate the ependymal wall through the interstitial cleft, a structure identified by MW. Brightman (1965; 2002) and can be captured by fractones (Kerever et al., 2007; Douet et al., 2012) to regulate adult neurogenesis (Douet et al., 2012; Douet et al., 2013).Since both fractones and SVZ blood vessels contain perlecan, it is likely to be involved in modulating signaling from the blood vessels and from the cerebrospinal fluid. We showed that FGF-2-promoted neurogenesis is impaired in the absence of perlecan. Taken together, these results strongly suggest that perlecan regulates neurogenesis by modulating the growth factor activity in the neurogenic niche. Our study revealed that perlecan is a critical extracellular matrix component of the neurogenic niche with multiple functions in development and in maintaining tissue.

Supplementary data to this article can be found online at http://dx.doi.org/10.1016/j.scr.2013.12.009.

Acknowledgments

This work was supported by grants from MEXT-Supported Program for the Strategic Research Foundation at Private Universities (2011–2015) and the Ministry of Education, Culture, Sports Science, and Technology of Japan (17082008 and 2230023 to E. A-H.) and the Intramural Program of the NIDCR, National Institutes of Health (Y.Y.). Bernard Zalc has received funding from the program "Investissements d'avenir" ANR-10-IAIHU-06.

References

Altman, J., 1963. Autoradiographic investigation of cell proliferation in the brains of rats and cats. Anat. Rec. 145, 573–591.

Altman, J., 1969. Autoradiographic and histological studies of postnatal neurogenesis. IV. Cell proliferation and migration in the anterior forebrain, with special reference to persisting neurogenesis in the olfactory bulb. J. Comp. Neurol. 137, 433–457.

Arikawa-Hirasawa, E., Koga, R., Tsukahara, T., Nonaka, I., Mitsudome, A., Goto, K., Beggs, A.H., Arahata, K., 1995. A severe muscular dystrophy patient with an internally deleted very short (110 kD) dystrophin: presence of the binding site for dystrophin-associated glycoprotein (DAG) may not be enough for physiological function of dystrophin. Neuromuscul. Disord. 5, 429–438.

Arikawa-Hirasawa, E., Watanabe, H., Takami, H., Hassell, J.R., Yamada, Y., 1999. Perlecan is essential for cartilage and cephalic development. Nat. Genet. 23, 354–358.

Arikawa-Hirasawa, E., Wilcox, W.R., Le, A.H., Silverman, N., Govindraj, P., Hassell, J.R., Yamada, Y., 2001. Dyssegmental dysplasia, Silverman-Handmaker type, is caused by functional null mutations of the perlecan gene. Nat. Genet. 27, 431–434.

Arikawa-Hirasawa, E., Le, A.H., Nishino, I., Nonaka, I., Ho, N.C., Francomano, C.A., Govindraj, P., Hassell, J.R., Devaney, J.M., Spranger, J., et al., 2002a. Structural and functional mutations of the perlecan gene cause Schwartz-Jampel syndrome, with myotonic myopathy and chondrodysplasia. Am. J. Hum. Genet. 70, 1368–1375.

Arikawa-Hirasawa, E., Rossi, S.G., Rotundo, R.L., Yamada, Y., 2002b. Absence of acetylcholinesterase at the neuromuscular junctions of perlecan-null mice. Nat. Neurosci. 5, 119–123.

Aviezer, D., Hecht, D., Safran, M., Eisinger, M., David, G., Yayon, A., 1994. Perlecan, basal lamina proteoglycan, promotes basic fibroblast growth factor-receptor binding, mitogenesis, and angiogenesis. Cell 79, 1005–1013.

Brightman, M.W., 1965. The distribution within the brain of ferritin injected into cerebrospinal fluid compartments. I. Ependymal distribution. J. Cell Biol. 26, 99–123.

Brightman, M.W., 2002. The brain's interstitial clefts and their glial walls. J. Neurocytol. 31, 595–603.

Chan, J.A., Balasubramanian, S., Witt, R.M., Nazemi, K.J., Choi, Y., Pazyra-Murphy, M.F., Walsh, C.O., Thompson, M., Segal, R.A., 2009. Proteoglycan interactions with Sonic Hedgehog specify mitogenic responses. Nat. Neurosci. 12, 409–417.

Corti, S., Nizzardo, M., Nardini, M., Donadoni, C., Locatelli, F., Papadimitriou, D., Salani, S., Del Bo, R., Ghezzi, S., Strazzer, S., et al., 2007. Isolation and characterization of murine neural stem/progenitor cells based on Prominin-1 expression. Exp. Neurol. 205, 547–562.

Costell, M., Gustafsson, E., Aszódi, A., Mörgelin, M., Bloch, W., Hunziker, E., Addicks, K., Timpl, R., Fässler, R., 1999. Perlecan maintains the integrity of cartilage and some basement membranes. J. Cell Biol. 147, 1109–1122.

Dey, A., She, H., Kim, L., Boruch, A., Guris, D.L., Carlberg, K., Sebti, S.M., Woodley, D.T., Imamoto, A., Li, W., 2000. Colony-stimulating factor-1 receptor utilizes multiple signaling pathways to induce cyclin D2 expression. Mol. Biol. Cell 11, 3835–3848.

Doetsch, F., García-Verdugo, J.M., Alvarez-Buylla, A., 1997. Cellular composition and three-dimensional organization of the subventricular germinal zone in the adult mammalian brain. J. Neurosci. 17, 5046–5061.

Doetsch, F., Caillé, I., Lim, D.A., García-Verdugo, J.M., Alvarez-Buylla, A., 1999. Subventricular zone astrocytes are neural stem cells in the adult mammalian brain. Cell 97, 703–716.

Douet, V., Arikawa-Hirasawa, E., Mercier, F., 2012. Fractone-heparan sulfates mediate BMP-7 inhibition of cell proliferation in the adult subventricular zone. Neurosci. Let. 528 (2), 120–125.

Douet, V., Kerever, A., Arikawa-Hirasawa, E., Mercier, F., 2013. Fractone-heparan sulphates mediate FGF-2 stimulation of cell proliferation in the adult subventricular zone. Cell Prolif. 46, 137–145.

Eriksson, P.S., Perfilieva, E., Björk-Eriksson, T., Alborn, A.M., Nordborg, C., Peterson, D.A., Gage, F.H., 1998. Neurogenesis in the adult human hippocampus. Nat. Med. 4, 1313–1317.

Fatrai, S., Elghazi, L., Balcazar, N., Cras-Méneur, C., Krits, I., Kiyokawa, H., Bernal-Mizrachi, E., 2006. Akt induces beta-cell proliferation by regulating cyclin D1, cyclin D2, and p21 levels and cyclin-dependent kinase-4 activity. Diabetes 55, 318–325.

Filla, M.S., Dam, P., Rapraeger, A.C., 1998. The cell surface proteoglycan syndecan-1 mediates fibroblast growth factor-2 binding and activity. J. Cell. Physiol. 174, 310–321.

Fischer, J., Beckervordersandforth, R., Tripathi, P., Steiner-Mezzadri, A., Ninkovic, J., Götz, M., 2011. Prospective isolation of adult neural stem cells from the mouse subependymal zone. Nat. Protoc. 6, 1981–1989.

Girós, A., Morante, J., Gil-Sanz, C., Fairén, A., Costell, M., 2007. Perlecan controls neurogenesis in the developing telencephalon. BMC Dev. Biol. 7, 29.

Hagihara, K., Watanabe, K., Chun, J., Yamaguchi, Y., 2000. Glypican-4 is an FGF2-binding heparan sulfate proteoglycan expressed in neural precursor cells. Dev. Dyn. 219, 353–367.

Ishijima, M., Suzuki, N., Hozumi, K., Matsunobu, T., Kosaki, K., Kaneko, H., Hassell, J.R., Arikawa-Hirasawa, E., Yamada, Y., 2012. Perlecan modulates VEGF signaling and is essential for vascularization in endochondral bone formation. Matrix Biol. 31, 234–245.

Kerever, A., Schnack, J., Vellinga, D., Ichikawa, N., Moon, C., Arikawa-Hirasawa, E., Efird, J.T., Mercier, F., 2007. Novel extracellular matrix structures in the neural stem cell niche capture the neurogenic factor fibroblast growth factor 2 from the extracellular milieu. Stem Cells 25, 2146–2157.

Kojima, T., Hirota, Y., Ema, M., Takahashi, S., Miyoshi, I., Okano, H., Sawamoto, K., 2010. Subventricular zone-derived neural progenitor cells migrate along a blood vessel scaffold toward the post-stroke striatum. Stem Cells 28 (3), 545–554.

Kowalczyk, A., 2004. The critical role of cyclin D2 in adult neurogenesis. J. Cell Biol. 167, 209–213.

Liu, G., Yuan, X., Zeng, Z., Tunici, P., Ng, H., Abdulkadir, I.R., Lu, L., Irvin, D., Black, K.L., Yu, J.S., 2006. Analysis of gene expression and chemoresistance of CD133+ cancer stem cells in glioblastoma. Mol. Cancer 5, 67.

Lois, C., Alvarez-Buylla, A., 1994. Long-distance neuronal migration in the adult mammalian brain. Science 264, 1145–1148.

Maric, D., Fiorio Pla, A., Chang, Y.H., Barker, J.L., 2007. Self-renewing and differentiating properties of cortical neural stem cells are selectively regulated by basic fibroblast growth factor (FGF) signaling via specific FGF receptors. J. Neurosci. 27, 1836–1852.

Mercier, F., Arikawa-Hirasawa, E., 2012. Heparan sulfate niche for cell proliferation in the adult brain. Neurosci. Lett. 1–6.

Mercier, F., Kitasako, J.T., Hatton, G.I., 2002. Anatomy of the brain neurogenic zones revisited: fractones and the fibroblast/macrophage network. J. Comp. Neurol. 451, 170–188.

Mercier, F., Kitasako, J.T., Hatton, G.I., 2003. Fractones and other basal laminae in the hypothalamus. J. Comp. Neurol. 455, 324–340.

Mirzadeh, Z., Merkle, F.T., Soriano-Navarro, M., Garcia-Verdugo, J.M., Alvarez-Buylla, A., 2008. Neural stem cells confer unique pinwheel architecture to the ventricular surface in neurogenic regions of the adult brain. Cell Stem Cell 3, 265–278.

Palmer, T.D., Ray, J., Gage, F.H., 1995. FGF-2-responsive neuronal progenitors reside in proliferative and quiescent regions of the adult rodent brain. Mol. Cell. Neurosci. 6, 474–486.

Palmer, T.D., Willhoite, A.R., Gage, F.H., 2000. Vascular niche for adult hippocampal neurogenesis. J. Comp. Neurol. 425, 479–494.

Pastrana, E., Cheng, L.C., Doetsch, F., 2009. Simultaneous prospective purification of adult subventricular zone neural stem cells and their progeny. Proc. Natl. Acad. Sci. 106 (15), 6387–6392.

Petreanu, L., Alvarez-Buylla, A., 2002. Maturation and death of adult-born olfactory bulb granule neurons: role of olfaction. J. Neurosci. 22, 6106–6113.

Raballo, R., Rhee, J., Lyn-Cook, R., Leckman, J.F., Schwartz, M.L., Vaccarino, F.M., 2000. Basic fibroblast growth factor (Fgf2) is necessary for cell proliferation and neurogenesis in the developing cerebral cortex. J. Neurosci. 20, 5012–5023.

Rapraeger, A.C., 1995. In the clutches of proteoglycans: how does heparan sulfate regulate FGF binding? Chem. Biol. 2, 645–649.

Seki, T., Arai, Y., 1993. Highly polysialylated neural cell adhesion molecule (NCAM-H) is expressed by newly generated granule cells in the dentate gyrus of the adult rat. J. Neurosci. 13, 2351–2358.

Shen, Q., Wang, Y., Kokovay, E., Lin, G., Chuang, S.-M., Goderie, S.K., Roysam, B., Temple, S., 2008. Adult SVZ stem cells lie in a vascular niche: a quantitative analysis of niche cell–cell interactions. Cell Stem Cell 3, 289–300.

Sirko, S., von Holst, A., Weber, A., Wizenmann, A., Theocharidis, U., Götz, M., Faissner, A., 2010. Chondroitin sulfates are required for fibroblast growth factor-2-dependent proliferation and maintenance in neural stem cells and for epidermal growth factor-dependent migration of their progeny. Stem Cells 28, 775–787.

Sun, Y., Kong, W., Falk, A., Hu, J., Zhou, L., Pollard, S., Smith, A., 2009. CD133 (prominin) negative human neural stem cells are clonogenic and tripotent. PLoS One 4, e5498.

Tavazoie, M., Van der Veken, L., Silva-Vargas, V., Louissaint, M., Colonna, L., Zaidi, B., Garcia-Verdugo, J.M., Doetsch, F., 2008. A specialized vascular niche for adult neural stem cells. Cell Stem Cell 3, 279–288.

Tsumaki, N., Tanaka, K., Arikawa-Hirasawa, E., Nakase, T., Kimura, T., Thomas, J.T., Ochi, T., Luyten, F.P., Yamada, Y., 1999. Role of CDMP-1 in skeletal morphogenesis: promotion of mesenchymal cell recruitment and chondrocyte differentiation. J. Cell Biol. 144, 161–173.

Uchida, N., Buck, D.W., He, D., Reitsma, M.J., Masek, M., Phan, T.V., Tsukamoto, A.S., Gage, F.H., Weissman, I.L., 2000. Direct isolation of human central nervous system stem cells. Proc. Natl. Acad. Sci. U. S. A. 97, 14720–14725.

Voigt, A., Pflanz, R., Schäfer, U., Jäckle, H., 2002. Perlecan participates in proliferation activation of quiescent Drosophila neuroblasts. Dev. Dyn. 224, 403–412.

Winner, B., Cooper-Kuhn, C.M., Aigner, R., Winkler, J., Kuhn, H.G., 2002. Long-term survival and cell death of newly generated neurons in the adult rat olfactory bulb. Eur. J. Neurosci. 16, 1681–1689.

Xu, Z., Ichikawa, N., Kosaki, K., Yamada, Y., Sasaki, T., Sakai, L.Y., Kurosawa, H., Hattori, N., Arikawa-Hirasawa, E., 2010. Perlecan deficiency causes muscle hypertrophy, a decrease in myostatin expression, and changes in muscle fiber composition. Matrix Biol. 29, 461–470.

Yayon, A., Klagsbrun, M., Esko, J.D., Leder, P., Ornitz, D.M., 1991. Cell surface, heparin-like molecules are required for binding of basic fibroblast growth factor to its high affinity receptor. Cell 64, 841–848.

Zhou, Z., 2004. Impaired angiogenesis, delayed wound healing and retarded tumor growth in perlecan heparan sulfate-deficient mice. Cancer Res. 64, 4699–4702.

BASIC RESEARCH PAPER

Autophagy 10:4, 1–11; April 2014; © 2014 Landes Bioscience

PARK2/Parkin-mediated mitochondrial clearance contributes to proteasome activation during slow-twitch muscle atrophy via NFE2L1 nuclear translocation

Norihiko Furuya,[1,†,‡,*] Shin-Ichi Ikeda,[2] Shigeto Sato,[3] Sanae Soma,[1] Junji Ezaki, [1] Juan Alejandro Oliva Trejo,[1] Mitsue Takeda-Ezaki,[1] Tsutomu Fujimura,[4] Eri Arikawa-Hirasawa,[3,5] Norihiro Tada,[5] Masaaki Komatsu,[6] Keiji Tanaka,[7] Eiki Kominami,[1] Nobutaka Hattori,[3] and Takashi Ueno[1,§,*]

[1]Department of Biochemistry; Juntendo University School of Medicine; Bunkyo-ku, Tokyo Japan; [2]Sportology Center; Juntendo University Graduate School of Medicine; Bunkyo-ku, Tokyo Japan; [3]Department of Neurology; Juntendo University School of Medicine; Bunkyo-ku, Tokyo Japan; [4]Laboratory of Proteomics and Biomolecular Science; Research Support Center; Juntendo University Graduate School of Medicine; Bunkyo-ku, Tokyo Japan; [5]Research Institute for Diseases of Old Age; Juntendo University Graduate School of Medicine; Bunkyo-ku, Tokyo Japan; [6]Protein Metabolism Project; Tokyo Metropolitan Institute of Medical Science; Setagaya-ku, Tokyo Japan; [7]Laboratory of Protein Metabolism; Tokyo Metropolitan Institute of Medical Science; Setagaya-ku, Tokyo Japan

Current affiliation: [†]Department of Research and Therapeutics for Movement Disorders; Juntendo University Graduate School of Medicine; Bunkyo-ku, Tokyo Japan; [‡]Department of Neurology; Juntendo University School of Medicine; Bunkyo-ku, Tokyo Japan; [§]Laboratory of Proteomics and Biomolecular Science; Research Support Center; Juntendo University Graduate School of Medicine; Bunkyo-ku, Tokyo Japan

Keywords: PARK2-mediated mitophagy, skeletal muscle atrophy, proteasome, NFE2L1, slow-twitch muscle, autophagy, mitochondria, knockout mouse

Abbreviations: ARE, antioxidant response element; CCCP, carbonyl cyanide m-chlorophenylhydrazone; NAC, N-acetyl-cysteine; NFE2L1, nuclear factor erythroid-derived 2-related factor 1; NFE2L2, nuclear factor erythroid-derived 2-related factor 2; ROS, reactive oxygen species; tBHQ, tert-butyl hydroquinone

Skeletal muscle atrophy is thought to result from hyperactivation of intracellular protein degradation pathways, including autophagy and the ubiquitin–proteasome system. However, the precise contributions of these pathways to muscle atrophy are unclear. Here, we show that an autophagy deficiency in denervated slow-twitch soleus muscles delayed skeletal muscle atrophy, reduced mitochondrial activity, and induced oxidative stress and accumulation of PARK2/Parkin, which participates in mitochondrial quality control (PARK2-mediated mitophagy), in mitochondria. Soleus muscles from denervated *Park2* knockout mice also showed resistance to denervation, reduced mitochondrial activities, and increased oxidative stress. In both autophagy-deficient and *Park2*-deficient soleus muscles, denervation caused the accumulation of polyubiquitinated proteins. Denervation induced proteasomal activation via NFE2L1 nuclear translocation in control mice, whereas it had little effect in autophagy-deficient and *Park2*-deficient mice. These results suggest that PARK2-mediated mitophagy plays an essential role in the activation of proteasomes during denervation atrophy in slow-twitch muscles.

Introduction

Skeletal muscles occupy up to 55% of total body mass in mammals, and generate motile forces and heat. They are a major site for carbohydrate and fatty acid metabolism and are categorized into 2 types exhibiting distinct contractile and metabolic properties: slow-twitch, oxidative fatigue-resistant muscles and fast-twitch, glycolytic fatigue-susceptible muscles. The slow-twitch muscle fibers typically display a 2- to 3-fold higher mitochondrial density and substantially lower capacity for nonoxidative ATP synthesis compared with the fast-twitch muscle fibers.

Maintenance of muscle mass depends on a balance between protein synthesis and degradation. Innervation of skeletal muscle fibers by motor neurons is essential for maintenance of muscle size, structure, and function. Numerous disorders, including amyotrophic lateral sclerosis, Guillain-Barre syndrome, polio, and polyneuropathy, disrupt the nerve supply to muscle, causing

*Correspondence to: Norihiko Furuya; Email: nohuruya@juntendo.ac.jp; Takashi Ueno; Email: upfield@juntendo.ac.jp
Submitted: 08/20/2013; Revised: 01/06/2014; Accepted: 01/09/2014
http://dx.doi.org/10.4161/auto.27785

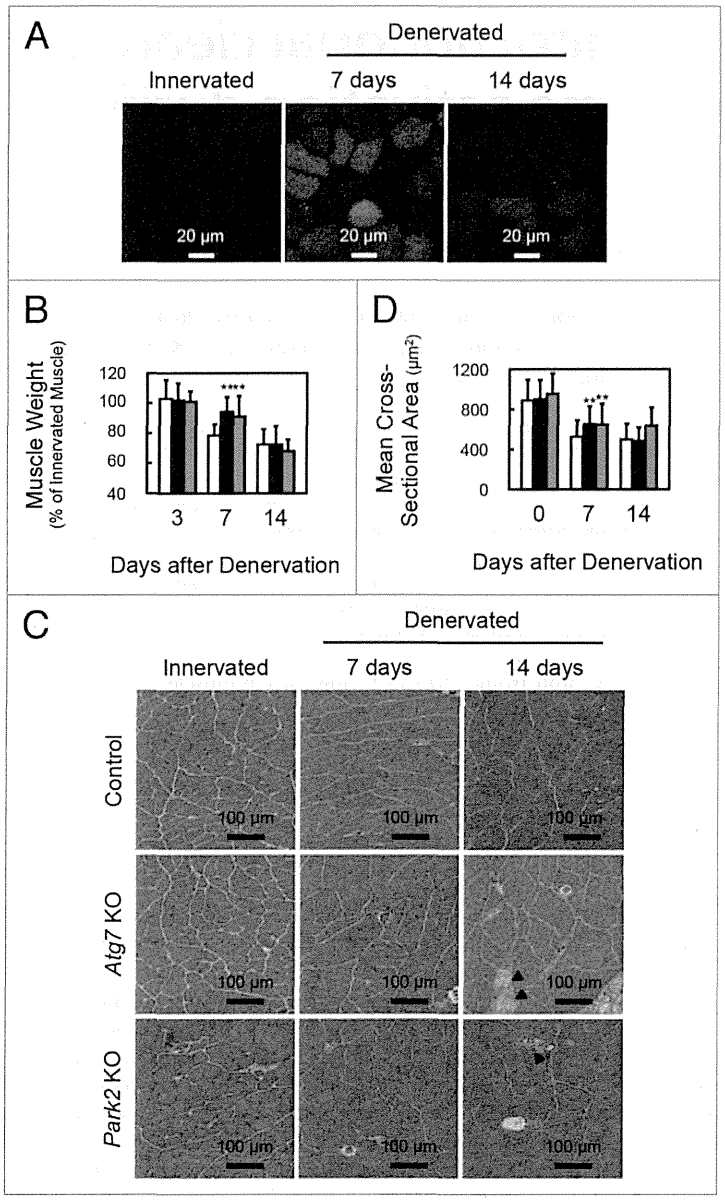

Figure 1. Delay of denervation atrophy in autophagy-deficient and PARK2-deficient soleus muscle. (**A**) Representative images of soleus muscles from GFP-LC3 transgenic mice at 0 (innervated), 7 and 14 d after denervation. Scale bar, 20 μm. (**B**) Time course of weight loss in the soleus muscles of denervated mice. For the denervation procedure, the left sciatic nerves of control mice (open bar: day 3, n = 9; day 7, n = 28; day 14, n = 19), *Atg7* KO mice (closed bar: day 3, n = 12; day 7, n = 30; day 14, n = 14) or *Park2* KO mice (gray bar: day 3, n = 3; day 7, n = 13; day 14, n = 7) were cut in the mid-thigh region, leading to denervation of the lower limb muscles. Denervated muscle weight data are shown as the percentage of the weight of the contralateral innervated muscle from the right limb. Data are shown as the means ± s.d. $^{**}P < 0.01$ vs control mice at the same time. (**C**) Histological analysis of control, *Atg7* KO and *Park2* KO soleus muscles. Cryosections were stained with hematoxylin and eosin. Arrowheads, dead myofibers. Scale Bars: 100 μm. (**D**) Quantification of the cross-sectional areas of myofibers. Values are the means ± s.d. vs control mice at the same time, $^{**}P < 0.01$.

loss of muscle mass strength and endurance (referred to as neurogenic atrophy).[1,2] Other pathological states and systemic disorders, including cancer, diabetes, fasting, sepsis, and disuse, also cause muscle atrophy. The resulting loss of muscle mass in these conditions involves an activation of intracellular protein degradation and a decrease in protein synthesis. The ubiquitin-proteasome system (UPS) and autophagy are the 2 major pathways leading to intracellular degradation, and, when upregulated by the activation of FOXO transcription factors, both systems can contribute to skeletal muscle atrophy.[3-6]

The UPS is responsible for biologically important cellular processes including cell cycle progression, DNA repair, signaling cascades, cell death, immunity, developmental programs, and protein quality control by catalyzing selective degradation of regulatory proteins and damaged proteins.[7,8] Macroautophagy (hereafter referred to as autophagy) is a membrane dynamic process in which cytoplasmic components including macromolecules and organelles are sequestered into double-membrane structures called autophagosomes and delivered to lysosomes for degradation.[9,10] Autophagy participates not only in supplying amino acids under nutrient-poor environments, but also in the clearance of misfolded or aggregated proteins, damaged organelles, and pathogens. Currently, the differences between the contributions of the UPS and autophagy to the process of muscle atrophy are not clear.

Results

Autophagy is required for the early steps of denervation atrophy in soleus muscle

To ascertain whether autophagy is activated in atrophying muscles, we subjected GFP-LC3 transgenic mice[11] to denervation of the sciatic nerve, a model of skeletal muscle atrophy (**Fig. 1A**; **Fig. S1A**). Many GFP-LC3 puncta were observed in both slow-twitch soleus muscles and fast-twitch plantaris muscles of mice at 7 and 14 d after denervation. In the initial stage (within 48 h) of denervation atrophy, autophagy is suppressed by the proteasome-dependent MTORC1 activation.[12] However, these results show that autophagy is activated in atrophying hind-limb muscles. As previously reported, autophagy deficiency in skeletal muscle causes more muscle loss owing to denervation than occurs in the control situation with normal autophagy, and autophagy is required to maintain muscle mass.[4] However the contribution of autophagy to the process of muscle atrophy is not clear. We generated mice with a skeletal muscle-specific *Atg7* (an essential gene for autophagy) knockout under the control of the tamoxifen-inducible human skeletal actin (HSA) promoter ($Atg7^{Flox/Flox}$: HSA-Cre-ER^{T2}, hereinafter referred to as *Atg7* KO mice), and subjected them to denervation. The plantaris muscles, a fast-twitch glycolytic skeletal muscle, from both *Atg7* KO and control ($Atg7^{Flox/Flox}$) mice, were atrophied to almost the same extent by denervation (**Fig. S1B**). In contrast, the soleus muscle, a slow-twitch oxidative skeletal muscle, from *Atg7* KO

mice, showed resistance to denervation at 7 d after denervation (**Fig. 1B–D**; **Fig. S2A**). However, the soleus muscles from *Atg7* KO mice and control mice exhibited comparable muscle mass and myofiber size at 14 d after denervation. Notably, dead myofibers were frequently observed in the *Atg7* KO soleus muscles at 14 d (**Fig. 1C**). The enhanced cell death at 14 d most likely contributes to the shrinking of the soleus muscle of *Atg7* KO mice. The phenotypes of soleus muscles of *Atg7* KO mice at 14 d after denervation are coincident with the previous study.[4] However, the phenotypes at a period earlier than 14 d after denervation were not investigated in that study. Thus, our finding seemed to reflect a more direct effect of autophagy-deficiency on muscle atrophy. These results indicated that autophagy contributes to the early stage of denervation atrophy and that autophagy deficiency delays atrophy in soleus muscle. In contrast, autophagy in fast-twitch muscles seems not to play an important role in the early stage of denervation atrophy, in spite of its activation by denervation in GFP-LC mice.

Denervated soleus muscle from *Atg7* KO mice shows mitochondrial dysfunction

To elucidate the precise phenotypes of the soleus muscles of denervated *Atg7* KO mice at 7 d after denervation, histological analyses were performed (**Fig. 2A**). The ratio of type I to type II muscle fibers in both innervated and denervated soleus muscles was almost the same in control and *Atg7* KO mice. Meanwhile, denervated soleus muscles from *Atg7* KO mice exhibited reduced staining for succinate dehydrogenase (SDH; complex II) and cytochrome *c* oxidase (Cox; complex IV) compared with denervated soleus muscles from control mice (**Fig. 2A and B**), indicating that the respiratory chain activities of denervated soleus muscles of *Atg7* KO mice were significantly decreased. The reduction of respiratory chain activities was not observed in denervated plantaris muscles from *Atg7* KO mice (**Fig. S1D**). As frequently reported for other autophagy-deficient mice, electron microscopy analysis revealed that abnormally swollen mitochondria were observed in the soleus muscles of denervated *Atg7* KO mice (**Fig. 2C**),[13-16] whereas, most of the mitochondria were morphologically normal in the soleus muscles of denervated *Atg7* KO mice. As was the case in GFP-LC3 mice, denervation induced formation of autophagic vacuoles (AVs) in the soleus muscles of control mice, whereas AVs were rarely observed in denervated soleus muscles of *Atg7* KO mice (**Fig. 2C**). These results indicated that autophagy deficiency leads to abnormal accumulation of mitochondria in the denervated soleus muscles. However, the expression levels of marker proteins for the outer membrane (e.g., TOMM20/Tom20), the intermembrane space (e.g., CYCS/cytochrome *c*), the inner membrane (e.g., OPA1), and the matrix (e.g., PDHA1/pyruvate dehydrogenase α1;) of mitochondria, and PPARGC1A/PGC1α, a master regulator of mitochondrial biogenesis, in denervated soleus muscles from *Atg7* KO mice, were comparable to those in the denervated muscles of control mice (**Fig. 2D**; **Fig. S2B**). The expression levels of DNM1L/Drp1 and FIS1/Fis1, which promote the fragmentation of mitochondria (Romanello et al., 2010), were not influenced by denervation. Mitochondrial DNA (mtDNA) copy numbers in denervated *Atg7* KO soleus muscles were not different from those in denervated control soleus muscles (**Fig. 2E**; **Fig. S2C**). Taken together, these results indicate that the decreased respiratory chain activities of denervated *Atg7* KO soleus muscle can be attributed to a qualitative reduction in mitochondrial function, but not to a decreased quantity of mitochondria. It is important to clarify the reason for the reduced mitochondrial function in denervated *Atg7* KO soleus muscles. Generally, oxidative stress is inseparably associated with dysregulation or disruption of mitochondrial functions, because mitochondria are both generators and targets of reactive oxygen species (ROS).[17] To ascertain whether ROS accumulate in denervated *Atg7* KO soleus muscles, we performed immunostaining with an antibody against 8-hydroxydeoxyguanosine (8-OHdG), a marker of ROS (**Fig. S3**). The denervated *Atg7* KO soleus muscles accumulated much more 8-OHdG than did the denervated control or the innervated *Atg7* KO soleus muscles. Moreover, the accumulation of carbonylated proteins was greater in denervated *Atg* KO soleus muscles than in denervated control or innervated *Atg7* KO muscles (**Fig. 2D**). These results suggest that denervated *Atg7* KO soleus muscles accumulate damaged mitochondria, which have reduced respiratory chain activities and produce abundant ROS.

PARK2 is required for denervation atrophy of soleus muscle

The E3 ubiquitin ligase PARK2/Parkin is commonly mutated in autosomal recessive juvenile parkinsonism.[18] Upon mitochondrial damage or uncoupling, PARK2 localizes to mitochondria and mediates the ubiquitination of mitochondrial outer membrane proteins and the autophagic elimination of damaged mitochondria (mitophagy), thereby participating in mitochondrial quality control.[19,20] Denervation induced PARK2 expression in hind-limb muscles (**Fig. 3A and B**; **Fig. S1C**) and the level of PARK2 expression induced by denervation was much higher in soleus muscles than in plantaris muscles. In addition to PARK2 expression, MFN1, a PARK2 substrate, accumulated in denervated soleus muscles from *Atg7* KO mice. In contrast, another E3 ubiquitin ligase, MUL1, which is involved in mitophagy during skeletal muscle atrophy,[21] was not induced by denervation in soleus and plantaris muscles. Subcellular fractionation experiments revealed that the mitochondrial fraction of the soleus muscles of denervated *Atg7* KO mice showed an accumulation of PARK2 (**Fig. 3C**). Immunofluorescence microscopy of cryosections of soleus muscles revealed colocalization of fragmented mitochondria and PARK2 in perinuclear regions of muscle fibers in denervated *Atg7* KO mice (**Fig. 3D**). These results indicate that damaged mitochondria associated with PARK2 are not eliminated and accumulate in the soleus muscles of denervated *Atg7* KO mice because of the deficiency of autophagy, and suggest that the contribution of PARK2 to mitochondrial clearance in denervated slow-twitch soleus muscles is much larger than it is in fast-twitch muscles, probably owing to the abundance of mitochondria. To confirm whether the PARK2-mediated mitophagy is involved in the denervation atrophy in the soleus muscles, we denervated *Park2*-deficient (*Park2* KO) mice.[22] Intriguingly, as was the case with *Atg7* KO mice, the soleus muscles from *Park2* KO mice retained muscle mass 7 d after denervation (**Fig. 1**). In

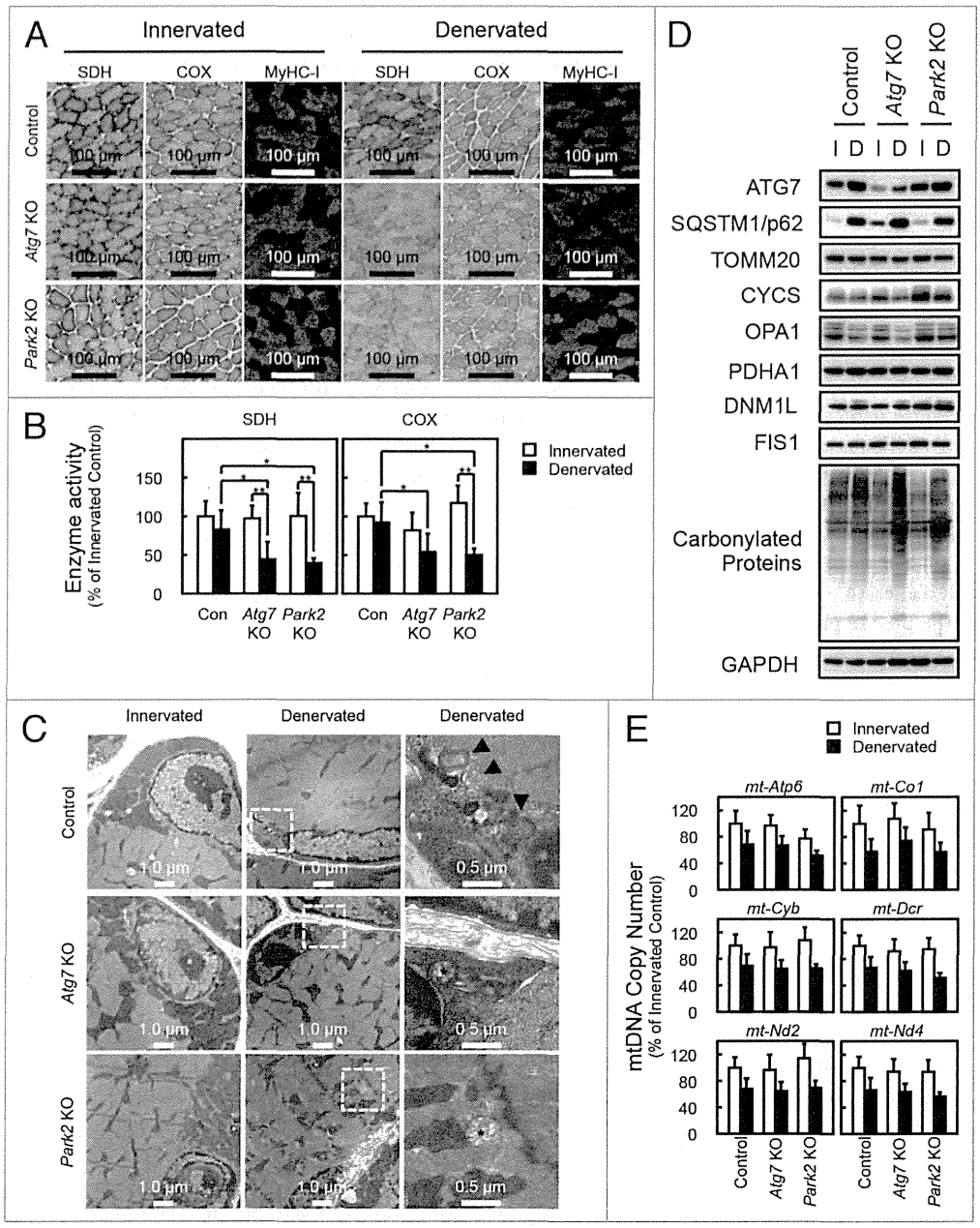

Figure 2. Denervation mediates mitochondrial damage in *Atg7* KO and *Park2* KO soleus muscles. (**A**) Histological analysis and immunofluorescence analysis of soleus muscles from control, *Atg7* KO and *Park2* KO mice 7 d after denervation. Histochemical detection of succinate dehydrogenase (SDH) and cytochrome *c* oxidase (COX) activities in cryosections of soleus muscles and immunofluorescence images of denervated soleus muscles stained with anti-myosin heavy chain I (MyHC-I, green) and anti-DMD (red) antibodies. Nuclei were visualized with Hoechst 33342 (blue). Scale bars, 100 μm. (**B**) Quantitative analysis of SDH and COX activities of soleus muscles shown in a. $^{*}P < 0.05$, $^{**}P < 0.01$. (**C**) Electron micrographs of control, *Atg7* KO and *Park2* KO soleus muscles at 7 d after denervation. Innervated limb and denervated limb are shown. The boxed regions in the middle panels are shown in the next panels on the right. Arrowhead, autophagic vacuole or phagophore membrane; asterisk, abnormal mitochondrion. (**D**) Western blot analysis of soleus muscles from mice at 7 d after denervation. Whole tissue lysates of the denervated (D) and the contralateral innervated (I) soleus muscles were immunoblotted with antibodies against the indicated proteins. The data shown are representative of at least 3 separate experiments. (**E**) Changes in mitochondrial DNA (mtDNA) copy numbers caused by denervation of soleus muscles. mtDNA copy numbers were quantified by real-time PCR to detect mtDNA-coded genes. Data are shown as the percentage of the values (mean ± s.d.) obtained from innervated soleus muscles from control mice.

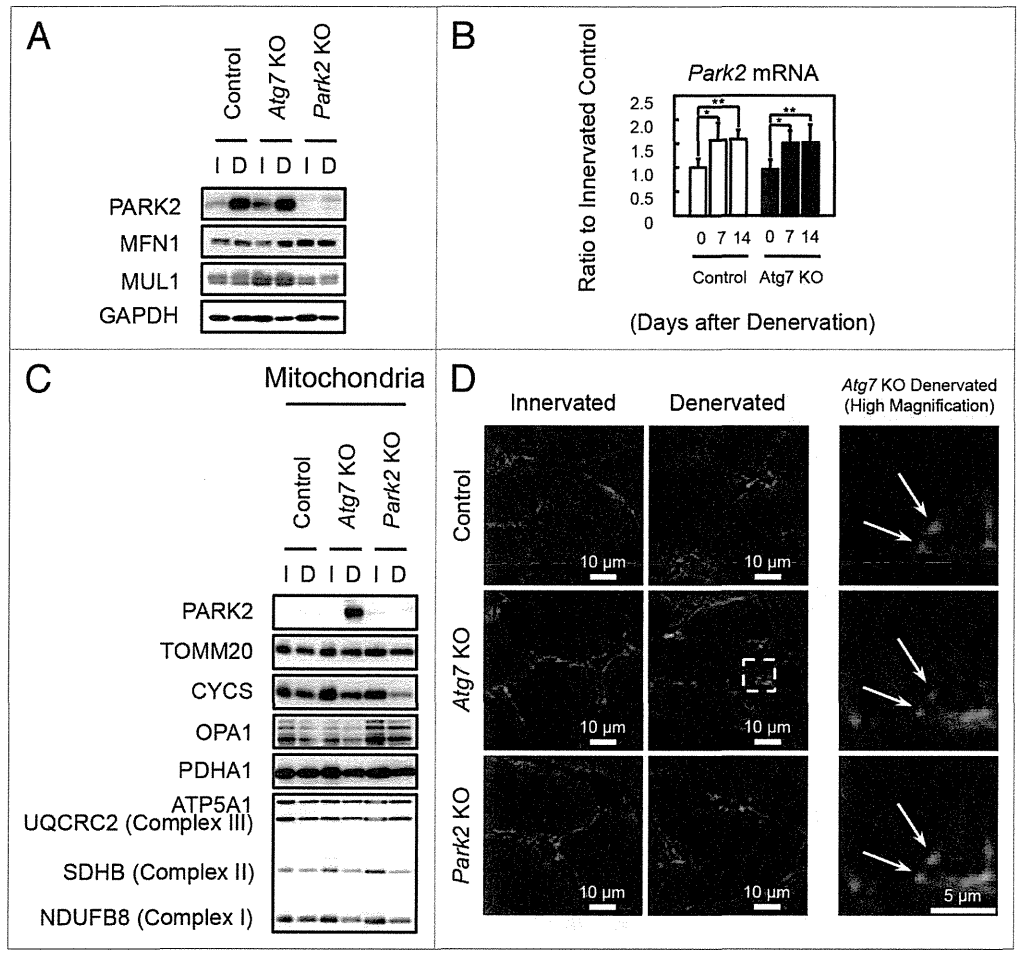

Figure 3. PARK2 accumulates in damaged mitochondria in denervated soleus muscles from *Atg7* KO mice. (**A**) Western blot analysis of soleus muscles from mice at 7 d after denervation with antibodies against the indicated proteins. (**B**) Quantification of *Park2* mRNA levels by real-time PCR in soleus muscles. Values are shown as ratios to the mRNA levels in innervated soleus muscles from control mice. The data are means ± s.d. vs. innervated (day 0) muscle from each genotype, $^{**}P < 0.01$. (**C**) Western blot analysis of mitochondrial fractions from soleus muscles. Mitochondrial fractions prepared from denervated (D) and innervated (I) soleus muscles of the indicated genotypes at 7 d after denervation and immunoblotted with anti-PARK2 antibody and antibodies against mitochondrial markers. (**D**) Immunofluorescent micrographs of denervated (7 d) or innervated soleus muscles of the indicated genotypes stained with anti-PARK2 (red) or anti-TOMM20 (mitochondrial marker, green) antibodies and Hoechst 33342 (nucleus, blue). Colocalization of fragmented mitochondria with PARK2 was observed in denervated *Atg7* KO soleus muscles. Boxed areas in denervated soleus muscles are shown in the next panels on the right.

addition, a reduction in their mitochondrial respiratory chain complex activities and accumulation of ROS were observed 7 d after denervation (**Fig. 2A–C**; **Fig. S3**). Together, these results indicate that the PARK2-mediated mitochondrial quality control pathway is required for the early stage of denervation atrophy of soleus muscles. A *Drosophila parkin*-null mutant shows obvious phenotypes including locomotive defects, muscle degeneration, and mitochondrial swelling in the flight muscles.[23-25] Indirect flight muscles, a group of specialized muscles with high mitochondria content, require a high oxygen supply to sustain their respiratory activity for a constant vibration. In mammals, slow-twitch muscles also contain more mitochondria than fast-twitch muscles. Thus, it is possible that mitochondria-rich muscles are more susceptible to the lack of PARK2-mediated mitophagy than other tissues.

PARK2-mediated mitophagy is required for proteasomal activation in denervated soleus muscle

To evaluate the mechanism underlying the delay of soleus muscle atrophy in denervated *Atg7* KO and *Park2* KO mice, we initially assumed the participation of the GDF8/myostatin signaling pathway and anti-apoptotic BCL2 family members in those phenotypes. However, denervation of wild-type, *Atg7* KO, and *Park2* KO mice resulted in very similar expression patterns for myostatin, myostatin receptor, and BCL2 family members in soleus muscles, indicating that none of these was related to the mechanism of atrophy (**Fig. S2B and S2D**). Finally, we noticed the accumulation of polyubiquitinated proteins in the soleus muscles of denervated *Atg7* KO and denervated *Park2* KO mice (**Fig. 4A**). In addition, the soleus muscles of denervated *Atg7* KO and *Park2* KO mice accumulated more polyubiquitinated proteins than did

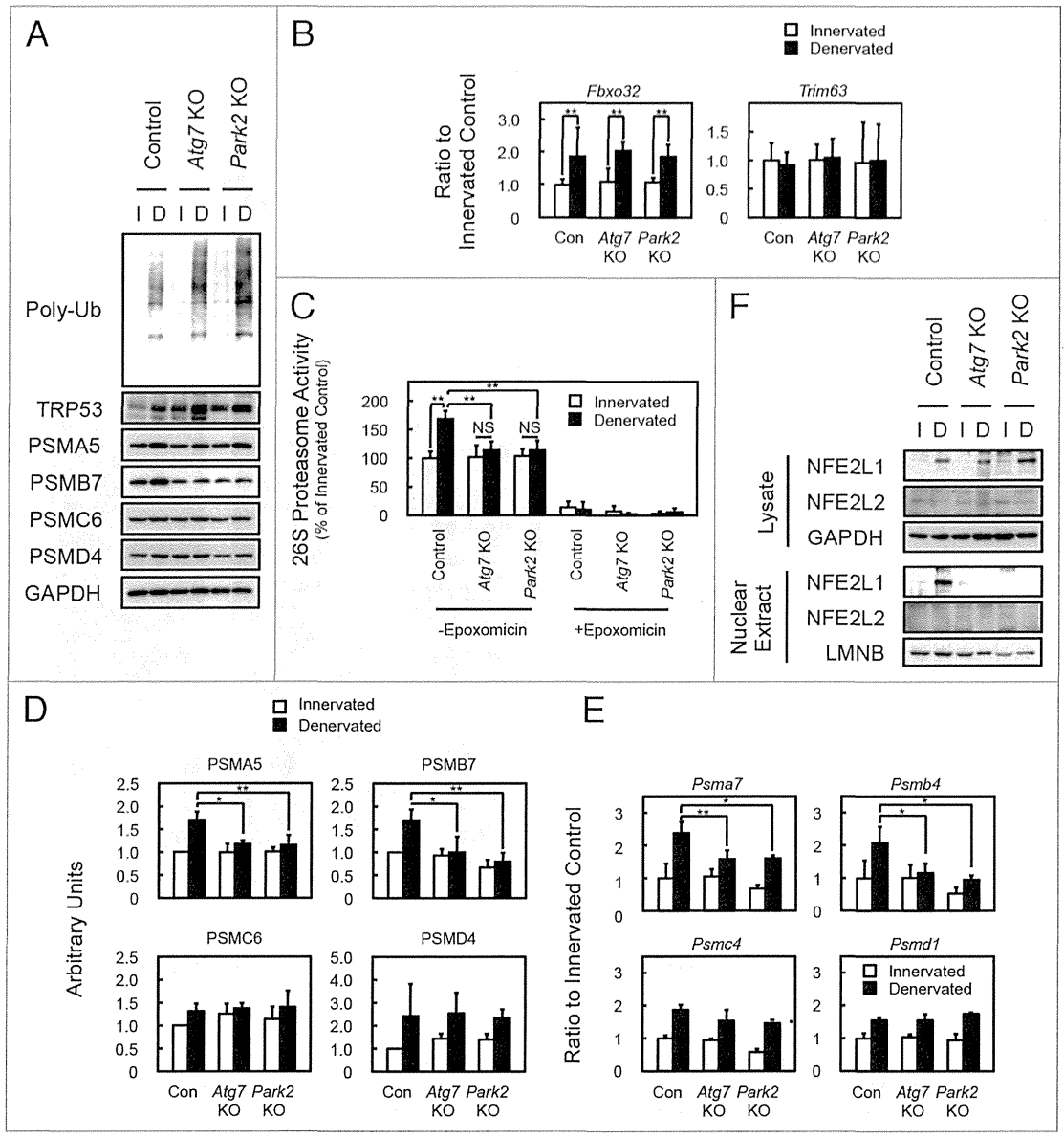

Figure 4. PARK2-mediated mitophagy is required for the activation of 26S proteasomes in denervated soleus muscle. (**A**) Western blot analysis of soleus muscles. Whole-tissue lysates of soleus muscles were immunoblotted with antibodies against the indicated proteins. The data shown are representative of at least 3 separate experiments. (**B**) Quantification of the mRNA levels for atrophy-related E3 ubiquitin ligases (*Fbxo32* and *Trim63*) in soleus muscles by real-time PCR. Data are shown as the ratios (mean ± s.d.) to the mRNA levels obtained from innervated soleus muscles from control mice. $^{**}P < 0.01$. (**C**) Peptide hydrolysis activity of 26S proteasomes. Soleus muscle homogenates from *Atg7* KO, *Park2* KO, and control mice were used to assay the chymotryptic activity of proteasomes using Suc-LLVY-AMC as a substrate in the absence or presence of 20 μM epoxomicin. Data are shown as the percentage of the activity (mean ± s.d.) obtained from innervated soleus muscles from control mice. $^{**}P < 0.01$, NS; not significant. (**D**) Quantitative densitometry of immunoblotting data for the proteasome subunits shown in a. $^{*}P < 0.05$, $^{**}P < 0.01$. (**E**) Quantification of the mRNA levels of proteasome subunits in soleus muscles by real-time PCR. Data are shown as the ratios (mean ± s.d.) to the mRNA levels obtained from innervated soleus muscles from control mice. $^{*}P < 0.05$, $^{**}P < 0.01$ vs denervated muscle from control mice. (**F**) Nuclear levels of NFE2L1 in soleus muscles. Nuclear extracts prepared from denervated and innervated soleus muscles and total tissue lysates were immunoblotted with anti-NFE2L1, anti- NFE2L2, anti-LMNB (as a loading control for nuclear extracts), and GAPDH (as a loading control for tissue lysates) antibodies. The data shown are representative of at least 3 separate experiments.

the plantaris muscles of those animals (Fig. S4A). It has been reported that the accumulation of polyubiquitinated proteins is a hallmark of autophagy-deficient tissues,[13-16] whereas a similar accumulation has not been reported in *Park2*-deficient animals. It is also known that the accumulation of unfolded proteins or protein aggregates interferes with proteasome-mediated protein degradation.[26,27] Therefore, we suspected that the deficiency of PARK2-mediated mitophagy attenuates the activity of the UPS pathway and results in the delay of soleus muscle atrophy in both *Atg7* KO and *Park2* KO mice. Because muscle-specific E3

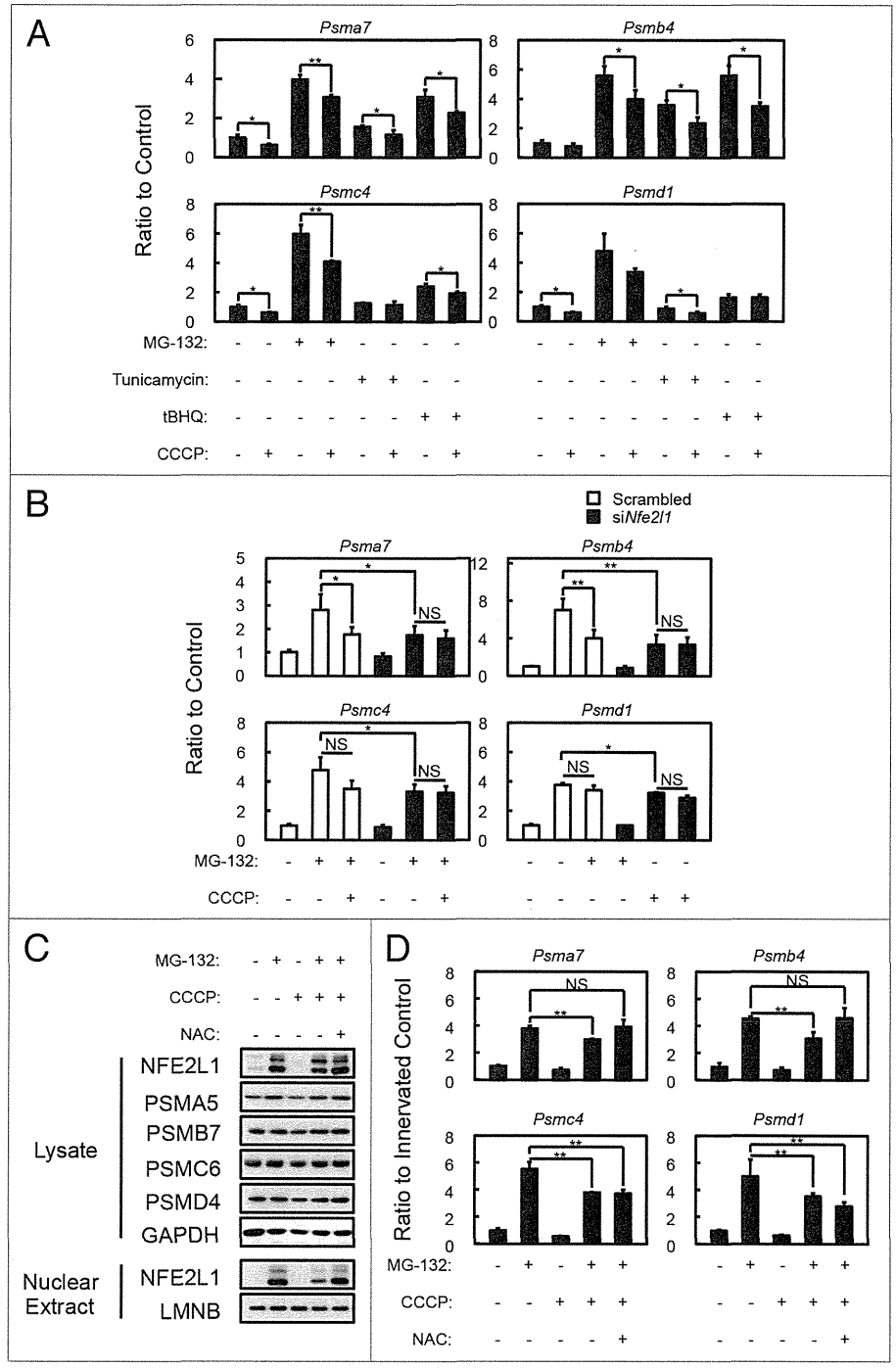

Figure 5. Effects of mitochondrial depolarization on proteasome subunit expression and NFE2L1 nuclear translocation in C2C12 cells. (**A**) Quantification of the mRNA levels of proteasome subunits in C2C12 cells incubated with 10 μM MG-132, 1 μg/ml tunicamycin and 50 μM tBHQ in the presence and absence of 10 μM CCCP for 24 h by real-time PCR. Data are shown as the ratios (mean ± s.d.) to the mRNA levels in the vehicle-treated control cells. $*P < 0.05$, $**P < 0.01$ (Student *t* test). (**B**) Quantification of the mRNA levels of proteasome subunits in si*Nfe2l1* treated C2C12 cells by real-time PCR. C2C12 cells were transfected with si*Nfe2l1* or scrambled siRNA, then incubated with 10 μM MG-132 in the presence and absence of 10 μM CCCP for 24 h. $*P < 0.05$, $**P < 0.01$, NS; not significant. (**C**) Western blot analysis of the cell lysates and nuclear extracts of C2C12 cells. Cell lysates and nuclear extracts of C2C12 cells incubated with 10 μM CCCP and/or 10 μM MG-132 in the presence or absence of 10 mM NAC for 24 h were assayed by western blotting using antibodies against the indicated proteins. The data shown are representative of at least 3 separate experiments. (**D**) Quantitative densitometry of immunoblotting data for the proteasome subunits shown in b. $**P < 0.01$, NS; not significant.

ubiquitin ligases are known to promote protein degradation during skeletal muscle atrophy,[28,29] we examined the expression levels of *Fbxo32/Mafbx/atrogin-1* and *Trim63/Murf1* using real-time quantitative PCR (**Fig. 4B**). However, the expression levels of *Fbxo32* and *Trim63* in denervated soleus muscles were comparable in all of the genotypes examined. Next, we measured 26S proteasomal activities in tissue extracts from denervated and innervated soleus muscles. In control mice, denervation induced 26S proteasome activities in extracts from soleus muscles. In contrast, denervation did not induce proteasomal activation in extracts from the soleus muscles of *Atg7* KO and *Park2* KO mice (**Fig. 4C**). In addition to proteasomal activities in vitro, we found that denervation increased the levels of the endogenous proteasome substrate TRP53/p53 in the soleus muscles of *Atg7* KO and *Park2* KO mice compared with those in controls (**Fig. 4A**). In the plantaris muscles of all genotypes examined, denervation did not induce the accumulation of TRP53 as in the soleus muscles of *Atg7* KO and *Park2* KO mice (**Fig. S4A**). These results suggest that, owing to a lack of proteasome activation after denervation in the soleus muscles of *Atg7* KO and *Park2* KO mice, more TRP53 accumulated, whereas proteasome activation in the soleus muscles of denervated control mice can result in lower levels of TRP53. To ascertain whether the difference in the amount of proteasome activation caused by denervation in control and KO soleus muscles is due to an increase in the number of proteasomes, we examined protein and mRNA levels for proteasome subunits. Western blot analysis revealed that expression of the subunits of 20S proteasomes (components of the

α and β rings) was more strongly induced by denervation in the soleus muscles of control mice than it was by denervation in the soleus muscles of *Atg7* KO and *Park2* KO mice (**Fig. 4A and D**). The mRNA levels for 20S proteasome subunits in the denervated soleus muscles from control mice were significantly higher than those in the denervated soleus muscles from *Atg7* KO and *Park2* KO mice (**Fig. 4E**). These results indicate that the deficiency of PARK2-mediated mitophagy suppresses denervation-induced transcription of 20S proteasome subunit mRNA as well as the de novo synthesis of proteasomes in soleus muscles. Interestingly, denervation induced the expression of proteasome subunits in the plantaris muscle of all genotypes examined (**Fig. S4A**). Therefore, denervated plantaris muscles of *Atg7* KO mice atrophied to almost the same extent seen in denervated plantaris muscles of control mice (**Fig. S1A**).

Accumulation of damaged mitochondria suppresses NFE2L1 transcriptional activity

Nuclear factor erythroid-derived 2-related factors (Nrfs; NFE2L1/Nrf1/TCF11/LCRF1 and NFE2L2/Nrf2), cap'n'collar-type basic leucine zipper (CNC-bZip) protein family members, have been reported to regulate the transcription of proteasome subunits.[30-33] Nrfs bind to the antioxidant response element (ARE) in the promoters of its target genes.[34] The promoters of all mammalian proteasome subunits contain ARE or ARE-like sequences.[32] To ascertain whether there were any differences in the Nrfs levels of the soleus muscles of control and *Atg7* or *Park2* KO mice, we examined Nrfs levels in tissue lysates and the nuclear extracts of soleus muscles by western blotting analysis (**Fig. 4F**). Denervation elevated total NFE2L1 levels in the soleus muscles of all genotypes examined, whereas, the NFE2L1 level was high in the nuclear extracts of soleus muscles of denervated control mice, but very low in those of the innervated control and denervated *Atg7* or *Park2* KO mice. In contrast, little NFE2L2 was detected in total lysate and nuclear extracts from soleus muscles. However, denervation did not influence the NFE2L1 levels in tissue lysates, and decreased nuclear NFE2L1 levels in the plantaris muscles of all genotypes examined (**Fig. S4C**). Although total NFE2L2 levels in plantaris muscles were comparable to those in soleus muscles, denervation elevated the NFE2L2 level in nuclear extracts of the plantaris muscles of all genotypes examined. These results indicate that 2 different Nrfs, NFE2L1 and NFE2L2, are involved in the denervation-induced expression of proteasome subunits in slow-twitch soleus muscle and fast-twitch plantaris muscle, respectively.

To confirm that the accumulation of damaged (or uncoupled) mitochondria in the soleus muscles of denervated *Atg7* KO or *Park2* KO mice affects NFE2L1 nuclear translocation, we treated C2C12 cells, a murine myoblast cell line, with the mitochondrial uncoupler carbonyl cyanide m-chlorophenylhydrazone (CCCP) to induce a mimetic condition of damaged mitochondria accumulation, and examined its effect on NFE2L1 transcriptional activity. As previously reported, incubation with several drugs, including proteasome inhibitors (MG-132), tunicamycin and tert-butyl hydroquinone (tBHQ), promotes mRNA expression of proteasome subunits (especially 20S proteasome components)[32,33,35,36] (**Fig. 5A**), and the expression of the 20S proteasome subunits induced by those drugs was suppressed by the addition of CCCP. In addition, siRNA knockdown of *Nfe2l1* significantly suppressed MG-132-induced proteasome subunit expression (**Fig. 5B**) Moreover, MG-132-induced NFE2L1 nuclear translocation was also suppressed by the addition of CCCP in C2C12 and HeLa cells (**Fig. 5C and D**; **Fig. S5C**). In addition, the effects of CCCP on MG-132-induced NFE2L1 nuclear translocation and NFE2L1 target-gene expression were blocked by the addition of N-acetyl-cysteine (NAC), an antioxidant. These results indicate that 24 h CCCP treatment induces ROS production from mitochondria in addition to the mitochondrial depolarization. To confirm the effect of ROS on NFE2L1 nuclear translocation, we tested the effects of rotenone, a complex I inhibitor, antimycin, a complex III inhibitor, and H_2O_2 on nuclear levels of NFE2L1 (**Fig. S5A and S5B**). As expected, the addition of rotenone, antimycin or H_2O_2 suppressed the MG-132-induced NFE2L1 nuclear translocation, and the effects of those drugs were invalidated by the addition of NAC. Together, these results indicate that the accumulation of damaged mitochondria producing ROS negatively affects NFE2L1 translocation and the transcription of NFE2L1 target genes.

Discussion

Mitochondria have been postulated to play an important role in triggering signals that contribute to muscle atrophy.[37] In this study, we noticed that a similar pattern of mitochondrial dysfunction and soleus muscle atrophy in denervated autophagy-deficient and *Park2*-deficient mice, and showed the evidence for PARK2-mediated mitophagy playing the important roles in slow-twitch muscle atrophy, which is the first report showing the physiological role of the PARK2-mediated mitophagy in mammalian in vivo model. The accumulation of damaged mitochondria in the PARK2-mediated mitophagy deficient soleus muscle, interferes the expression of proteasome subunits (**Fig. S6**). The elevation of proteasome expression is the key event in the early stage of slow-twitch muscle atrophy, and that it is regulated by a transcription factor NFE2L1. Under nonstress conditions, NFE2L1 is targeted by its N-terminal putative transmembrane domain to the endoplasmic reticulum (ER) membrane, where it is quickly degraded via ER-associated degradation (ERAD).[33,35,38] In response to proteasome inhibition, NFE2L1 translocates from the ER to the nucleus, where it transactivates the transcription of target genes including proteasome subunits. Conversely, NFE2L2, another Nrfs, is constitutively degraded by proteasome because its binding partner KEAP1 (kelch-like ECH-associated protein 1) is a component of the ubiquitin ligase complex in standard conditions.[39-42] The oxidative and electrophilic stresses inactivate KEAP1 by the modification of its cysteine residues, and stabilize NFE2L2 to induce the transcription of numerous cytoprotective genes.[43-45] In this study, we showed that NFE2L1 nuclear translocation is interfered by oxidative stress, which activates NFE2L2 activity. Therefore, the PARK2-mediated mitochondrial quality control system plays an important role

in NFE2L1-dependent slow-twitch muscle atrophy, because of interference in the NFE2L1 system by oxidative stress. Furthermore, fast-twitch plantaris muscles atrophied same extent by denervation in the presence and the absence of PARK2-mediated mitophagy, express lower levels of PARK2 and NFE2L1 than slow-twitch muscles during denervation atrophy. Therefore, we speculate that tissues regulated by the NFE2L1 system express more PARK2 to eliminate damaged mitochondria than do other tissues. Our findings highlight the linkage between mitochondria autophagy and the UPS, 2 major intracellular protein degradation systems, and their different roles in slow-twitch skeletal muscle atrophy.

Materials and Methods

Antibodies and reagents

Anti-ATG7 antibodies were described previously.[14] Anti-PARK2 (Parkin, 4211), anti-PDHA1 (pyruvate dehydrogenase, 3205), anti-PSMD4 (Rpn10/S5a, 3846), anti-GAPDH (2118), anti-TRP53 (p53, 2524), anti-NFE2L1 (TCF11/Nrf1, 8052), anti-BCL2 (Bcl-2, 2870) and anti-BCL2L1 (Bcl-xL, 2764) antibodies were obtained from Cell Signaling Technology. Anti-PSMA5 (Proteasome 20S α5 subunit, BML-PW8125), anti-PSMB7 (Proteasome 20S β2 subunit, BML-PW9300) and anti-PSMC6 (Proteasome 19S Rpt4 subunit, BML-PW8830) were obtained from Enzo Life Sciences. Anti-OPA1 (612606) and anti-DNM1L (Drp1, 611112) were obtained from BD transduction laboratories. Anti-SQSTM1 (GP62-C) was obtained from Progen. Anti-MYH7(myosin heavy chain I, Clone NOQ7.5.4D, M8421) was obtained from Sigma-Aldrich. Anti-multi ubiquitin (Clone FK2, D058-3) was obtained from MBL. Anti-PPARGC1A (PGC-1, AB3242) was obtained from Millipore. MitoProfile Total OXPHOS Rodent WB Antibody Cocktail (MS604) was obtained from MitoSciences. Anti-TOMM20 (Tom20, sc-11415), anti-CYCS (Cytochrome *c*, sc-13156), anti-NFE2L1 (Nrf1, H-285, sc-13031, for immunostaining of HeLa cells), anti-NFE2L2 (Nrf2, H-300, sc-13032) and anti-LMNB (Lamin B, sc-6216) were obtained from Santa Cruz Biotechnology. Anti-DMD (Dystrophin, ab15277) and anti-MUL1 (ab84067) were obtained from Abcam. Anti-MFN1 (H00055669-M04) was obtained from Abnova. Anti-FIS1 (10956-1-AP) was obtained from Proteintech. Anti-8-OHdG (MOG-020P) was obtained from the Japan Institute for the Control of Aging, NIKKEN SEIL Co, Ltd. The Protein Carbonyls Western Blot Detection Kit was obtained from SHIMA Laboratories. Alexa 488- and Alexa 594-conjugated secondary antibodies (A11034, A11029, A11037, A11032) were obtained from Molecular Probes. The M.O.M. Immunodetection kit and Texas Red Avidin DCS were obtained from VECTOR Laboratories. Tunicamycin (T7765), tBHQ (112941), CCCP (C-2759), rotenone (R-8875), antimycin (A-8674) and N-acetyl-cysteine (A9165) were obtained from Sigma-Aldrich. MG-132 (474790) was obtained from CALBIOCHEM. Succinyl-Leu-Leu-Val-Tyr-7-amido-4-methylcoumarin (Suc-LLVY-MCA, 3120-v) and epoxomicin (4381-v) were obtained from Peptide Institute, Inc.

Animals

HSA-Cre-ER^{T2} transgenic mice were a gift from Dr Pierre Chambon. To produce *Atg7*$^{Flox/Flox}$: HSA-ER^{T2}-Cre mice, *Atg7*$^{Flox/Flox}$ mice were bred with HSA-Cre-ER^{T2} transgenic mice. To delete the floxed *Atg7* gene from skeletal muscle, Cre-ER^{T2} recombinase activity was induced in 4-wk-old mice by i.p. injections of 1 mg tamoxifen for 5 consecutive days. GFP-LC3 transgenic and *Park2* knockout mice have been previously described. All mice were maintained in an environmentally controlled room (lights on from 8:00 to 20:00) and were fed a pelleted laboratory diet and tap water ad libitum, unless otherwise stated. Denervation was performed at 4 wk after tamoxifen injections. To standardize autophagic activity in the skeletal muscles, mice were fasted for 24 h before euthanasia. Experimental protocols were approved by the Ethics Review Committee for Animal Experimentation of Juntendo University.

Histological analysis and electron microscopy

Cryosections, 10 μm thick, from mouse hind limbs were stained with hematoxylin and eosin (H&E), stained for succinate dehydrogenase (SDH) or cytochrome *c* oxidase (COX) activities, or immunolabeled with anti-PARK2, anti-TOMM20, anti-myosin heavy chain I (MYH7), anti-DMD and anti-8-OHdG antibodies. To quantify the SDH or COX activities of soleus muscles, Image J software was used. For EM analysis, soleus muscles were directly fixed with 2% glutaraldehyde in 0.1 M cacodylate buffer on ice. Embedding, sectioning and microphotography were performed by the Hanaichi Electron Microscopic Laboratory, Inc.

Cell culture and siRNA transfection

C2C12 cells and HeLa cells were maintained in DMEM supplemented 10% fetal calf serum and antibiotics. For RNA interference experiments, ON-TARGETplus mouse *Nfe2l1* siRNA (Thermo Scientific Dharmacon, L-062252-01-0005) or nontargeting controls (Thermo Scientific Dharmacon, D-001810-01-05) were transfected into C2C12 cells using Lipofectamine RNAiMAX reagent according to the manufacturer's protocols (Invitrogen, 13778075).

Isolation of mitochondrial fractions and nuclear extracts

Mitochondrial fractions of soleus muscles were isolated using the Mitochondria Isolation Kit for Tissue (Pierce, 89801), and nuclear extracts of soleus muscles or C2C12 cells were prepared using NE-PER Nuclear and Cytoplasmic Extraction Reagents (Pierce, 78833) according to the manufacturer's protocols.

Western blotting

For tissue lysate preparation, mouse skeletal muscles were homogenized in 10 volumes of 50 mM TRIS-HCl (pH 7.4) containing 0.15 M NaCl, 1 mM EDTA, 1% Triton X-100, 0.5% sodium deoxycholate, 0.1% SDS, a protease inhibitor cocktail (Roche Diagnostics, 11836170001), and a phosphatase inhibitor cocktail (Roche Diagnostics, 04906837001), using a motor-driven homogenizer (As One, S-203). For C2C12 cell lysate preparation, cells were lysed with the same buffer. The lysates were centrifuged at 12,000 × *g* for 10 min at 4 °C to remove debris. The supernatants, mitochondrial fractions, or nuclear extracts were analyzed by western blotting. Densitometric analysis was performed using ImageJ software.